applied sciences

MDPI

Article

Numerical Simulation of the Dynamic Response of a Geocell-Reinforced Aeolian Sand Roadbed Under Vehicle Driving Conditions

Jie Liu [1,2,3], Jinchao Kong [1,2,3], Jiapeng Xia [1,2,3], Ya Yang [1,2], Jiadong Pan [1,2,4,5,*] and Jing Zhang [1,2,3,5,*]

1 Xinjiang Transportation Science Research Institute Co., Ltd., Urumqi 830000, China
2 Xinjiang Key Laboratory of Highway Engineering Technology in Arid Desert Areas, Urumqi 830000, China
3 College of Transportation and Logistics Engineering, Xinjiang Agricultural University, Urumqi 830052, China
4 State Key Laboratory of Geomechanics and Geotechnical Engineering Safety, Institute of Rock and Soil Mechanics, Chinese Academy of Sciences, Wuhan 430071, China
5 University of Chinese Academy of Sciences, Beijing 100049, China
* Correspondence: pjd_chd@163.com (J.P.); zhangjing245@mails.ucas.ac.cn (J.Z.)

Highlights

- Q: How is the dynamic response of geocell-reinforced aeolian sand subgrades captured? A: By a validated 3D finite element model.
- Q: Which factors significantly affect dynamic stress distribution within the subgrade? A: Vehicle speed and weight.
- Q: How does geocell reinforcement affect dynamic stress? A: It reduces peak dynamic stress and improves stress-distribution uniformity.
- Q: What mechanisms explain reinforcement under moving vehicle loads? A: The confinement and net effects.

Abstract

To investigate the dynamic response and reinforcement mechanism of geocell-reinforced aeolian sand roadbeds under vehicle loading, a three-dimensional finite element model incorporating vehicle body–wheel–road coupling dynamics was established and validated using field driving tests with a 43-t truck traveling at 20 and 60 km/h. Further numerical simulations investigated the effects of vehicle mass (25–49 t) and driving speed (20–100 km/h). The results show that dynamic stress decreases with increasing depth, with an attenuation of 81.8–89.9% over the investigated 0.96 m thick roadbed structure. Dynamic stress increases with vehicle mass but decreases with driving speed under the investigated numerical conditions. Compared with the conventional gravelly soil roadbed, the geocell-reinforced aeolian sand roadbed exhibits lower dynamic stresses and a more uniform stress distribution. Furthermore, the maximum deviations between the numerical simulations and field measurements were approximately 4.6–4.8% under the field-tested conditions, indicating good agreement. These findings provide a reference for the application of geocell-reinforced aeolian sand in desert highway construction.

Keywords: geocell; aeolian sand; dynamic response of the roadbed; numerical simulation

Check for updates

Academic Editor: Francesco Zirilli

Received: 29 October 2026
Revised: 18 November 2026
Accepted: 19 November 2026
Published: 24 November 2026

Copyright: © 2026 by the authors. Licensee MDPI, Basel, Switzerland. This article is an open access article distributed under the terms and conditions of the Creative Commons Attribution (CC BY) license.

1. Introduction

The use of geocells as a reinforcement material for improving soil conditions has wide application prospects in areas such as highways and railways [1–4]. The dynamic performance of soil-reinforced embankments directly affects their long-term dynamic stability.

Clarifying the dynamic load transfer mechanism between each structural layer is the key to improving the service performance of an embankment; however, the dynamic response of a soil-reinforced roadbed with a geocell is influenced by its unique structural form and the superimposed effect of wheel loads, and the dynamic behavior within each structural layer and its attenuation process exhibit nonlinearity [5]. Desert roads often experience uneven settlement due to insufficient bearing capacity, which significantly affects the service performance of the roadbed. Therefore, desert highways have strict requirements for the long-term stability of the direct supporting structure (subgrade) of the road surface.

Based on theoretical analysis, numerical simulation, indoor model tests and other research methods, many researchers have carried out extensive and in-depth studies on the reinforcing effect of geocells and their stress diffusion behavior and found that the reinforcing effect of geocells is mainly manifested in the improvement in foundation bearing capacity, reduction in foundation settlement and surface uplift, etc. [6–9]. Moreover, aeolian sand, which is widely distributed in desert areas with abundant reserves and good water stability, has been extensively used as a fill material for desert highway subgrades in engineering projects. The reinforcement of aeolian sand with geocells has shown excellent effects and is convenient for desert transportation, road construction due to the superior mechanical performance, on-site material sourcing, cost savings, and rapid construction practices of geocells [10]. Gao et al. [11]. Conducted vibration response tests on two types of upper roadbed structures reinforced with geocells for aeolian sand and gravel soil subgrades. They studied the reinforcement effect of geocells on aeolian sand subgrades through field experiments and theoretical analysis. Latha et al. [12] used model tests and finite element analysis to study the settlement deformation characteristics of reinforced sand cushions, geocell gravel cushions, and unreinforced road subgrades under static and cyclic loads on foundation surfaces and compared the effects of factors such as the geocell size, stiffness, and number of layers on improving the bearing capacity of foundations. Saride [13] demonstrated through numerical simulation and laboratory experiments that geocells play a role in pressure diffusion. A. Hegde [14–16] performed model tests and concluded that the addition of geocells increases the ultimate bearing capacity of aeolian sand layers by 2.4–3.2 times and verified the experimental research through three-dimensional modeling, further concluding that geocells spread the load laterally to a wider area below the structural layer. In addition, focusing on the mechanical properties of aeolian sand, Zhang et al. [17]. Conducted indoor geotechnical tests on aeolian sand in the three Chinese provinces of Xinjiang, Inner Mongolia, and Shaanxi, followed by California bearing ratio (CBR), rebound, compression, and shear tests, to comprehensively study the static properties of aeolian sand as a subgrade fill material. Li et al. [18]. Systematically analyzed the particle size, compaction characteristics, dynamic properties, and settlement characteristics of aeolian sand construction and proposed a method for the dry compaction of building subgrades, while using geotextile fabric to isolate the aeolian sand subgrade from the upper road surface structure, which has become the most widely used engineering technology in desert road projects.

Most of the research on geocell chambers mentioned above has focused on static loads. However, during the operational lifespan of highways, geocell-reinforced roadbeds inevitably experience complex dynamic loads from vehicles. Venkateswarlu [19] performed a three-dimensional numerical simulation study on the reinforcement of a foundation cushion layer using a geocell. This study compared the performance of a geocell reinforced cushion layer with that of an unreinforced cushion layer and evaluated the vibration isolation potential of the geocell. Wu [20] studied the dynamic characteristics of geocell-reinforced RSM under cyclic loading through large-scale cyclic shear tests. The addition of the geocell restricted the development of shear bands and promoted uniform shear deformation

throughout the height of the specimen. The dynamic characteristics with reinforcement were more stable than the dynamic characteristics without reinforcement. Tafreshi [21] conducted model experiments to compare the static and cyclic load responses of reinforced sandy soil foundations with geocell confinement and found that plastic deformation is more restricted by geocell confinement under dynamic loading than under similar static loading conditions. Suku [22] studied the reinforcement effect of geocell chambers through repeated loading tests with a uniformly distributed load on a plate and observed that the geocell chambers can effectively reduce permanent deformation. Siabil [23] investigated the suitability of geocell reinforcement for reducing rutting depth, surface settlement, and/or pavement cracking during the lifespan of pavement supported by expanded polystyrene (EPS) geofoam blocks through a series of large-scale cyclic plate load tests and simplified numerical simulations. It was found that the efficiency of geocell reinforcement under cyclic dynamic loads depends on the magnitude of applied pressure, as increasing the amplitude of cyclic pressure can enhance the benefits of geocell reinforcement. Yang [24] conducted model tests to study vehicle acceleration on a road with an unreinforced sand subgrade of geocell chambers. The results showed that the geocell chambers significantly improved the stability of the sand subgrade and reduced the formation of ruts. Tavakoli [25] conducted a cyclic loading test on a road model with pipeline crossing using geocell-reinforced pavement. It was found that compared with the unreinforced model, the road model with geocell-reinforced chambers reduced the soil pressure [26,27]. The deflection of the geocell-reinforced bed with a pipeline was approximately one-third of the allowable value, indicating that geocell reinforcement can provide safe conditions for pipelines, even under strong repetitive loads such as busy traffic. Most of the dynamic loads considered in these studies are single dynamic loads, and the dynamic superposition effect of multiple vehicle wheels has not been accounted for [28]. Nevertheless, most studies focused either on static loads or simplified cyclic loads, often neglecting multi-wheel dynamic superposition and the specific behavior of aeolian sand as a subgrade material. In northwestern China, where desertification is severe and aeolian sand is widely distributed, the loose particles have insufficient bearing capacity, requiring innovative solutions. Few works have quantitatively assessed the attenuation and homogenization effects of geocell-reinforced aeolian sand under real vehicle traffic conditions.

To address these research gaps, this study establishes a three-dimensional vehicle–tire–roadbed coupled finite element model to investigate the dynamic response of geocell-reinforced aeolian sand roadbeds under moving multi-wheel vehicle loads. The model is validated using field driving tests conducted on the S21 Desert Highway. The specific objectives are to (1) evaluate the dynamic stress transmission and attenuation characteristics of the roadbed under different vehicle masses and traveling speeds; (2) compare the dynamic stress distribution of conventional gravel–soil and geocell-reinforced aeolian sand roadbeds; and (3) investigate the dynamic deformation of geocells and their reinforcement mechanisms, particularly the confinement and net effects. Compared with previous studies primarily based on static or simplified cyclic loading, this study incorporates vehicle–tire–roadbed coupling and moving multi-wheel loading, together with field validation, to provide a more comprehensive understanding of dynamic stress redistribution and geocell reinforcement mechanisms in aeolian sand roadbeds.

2. Materials and Methods

2.1. Materials

2.1.1. Soil Material

Typical aeolian sand zones from different regions of the Beijiang Guerbantonggute Desert were selected and transported to the laboratory. After natural air drying, the soil

samples were sieved through a 2 mm round-hole sieve to remove impurities such as gravel and deadwood. The sieved soil samples were then placed in an oven at 105 °C for a minimum of 24 h to complete the drying process. The dried soil samples were subjected to particle size distribution tests according to the Highway Geotechnical Testing Procedures (JTG 3430-2020) [29], and the test results are shown in Table 1. The soil gradation curve is shown in Figure 1.

Table 1. Aeolian sand grain gradation table.

Particle size/mm	<0.075	0.075~0.1	0.1~0.25	0.25~0.5	0.5~1
proportion/%	4	19.1	68.2	8.2	0.5

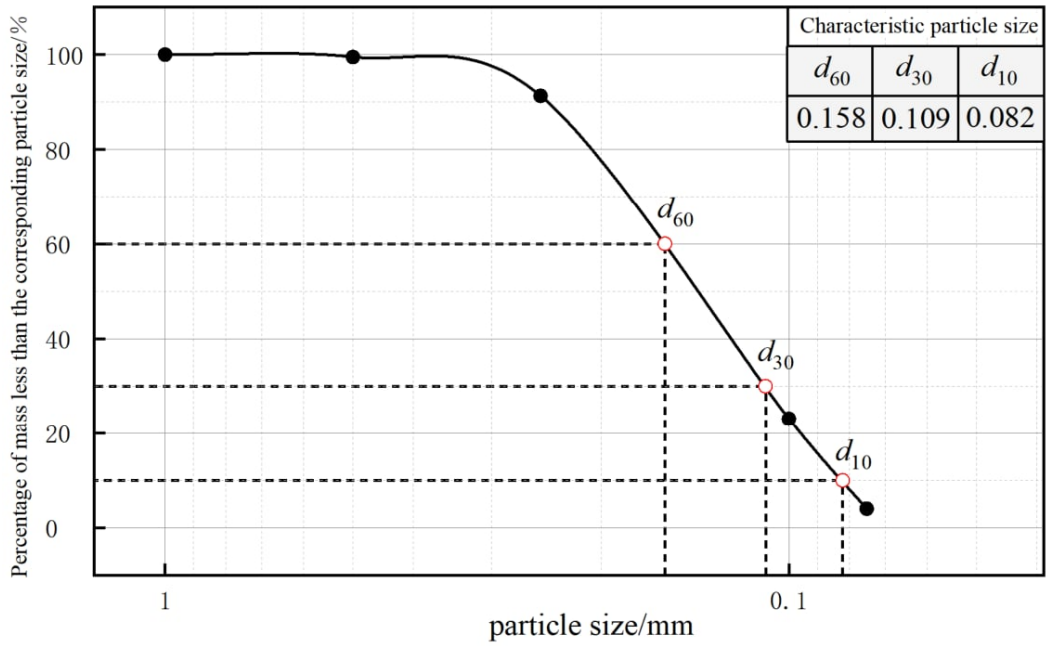

Figure 1. Grain size gradation accumulation curve of aeolian sand.

To analyze the distribution of the wind-eroded sand particle grain size, according to the grading curve calculation, Cu = 1.93 and Cc = 0.92 are obtained. Based on this, it can be concluded that the particle size distribution of the aeolian sand is discontinuous (Cc ≤ 1 or Cc ≥ 3) and that the grading is uniform (Cu < 5), with a main particle size distribution between 0.075 mm and 0.25 mm, corresponding to over 80% of the sample. This indicates that the aeolian sand is poorly graded fine sand, which is different from the typical backfill material used for retaining walls. Therefore, special construction techniques or structural designs need to be adopted when using aeolian sand for filling retaining walls.

Determining the maximum dry density and optimum moisture content of the soil after compaction is the basis for the construction control and quality evaluation of roadbed fill. Starting from a moisture content of 0%, 12 groups of soil samples with different moisture contents, following a moisture content increment of 1.5%, were prepared for compaction tests. After the completion of the tests, the density and moisture content of the soil samples were measured, and the compaction curve was plotted, as shown in Figure 2.

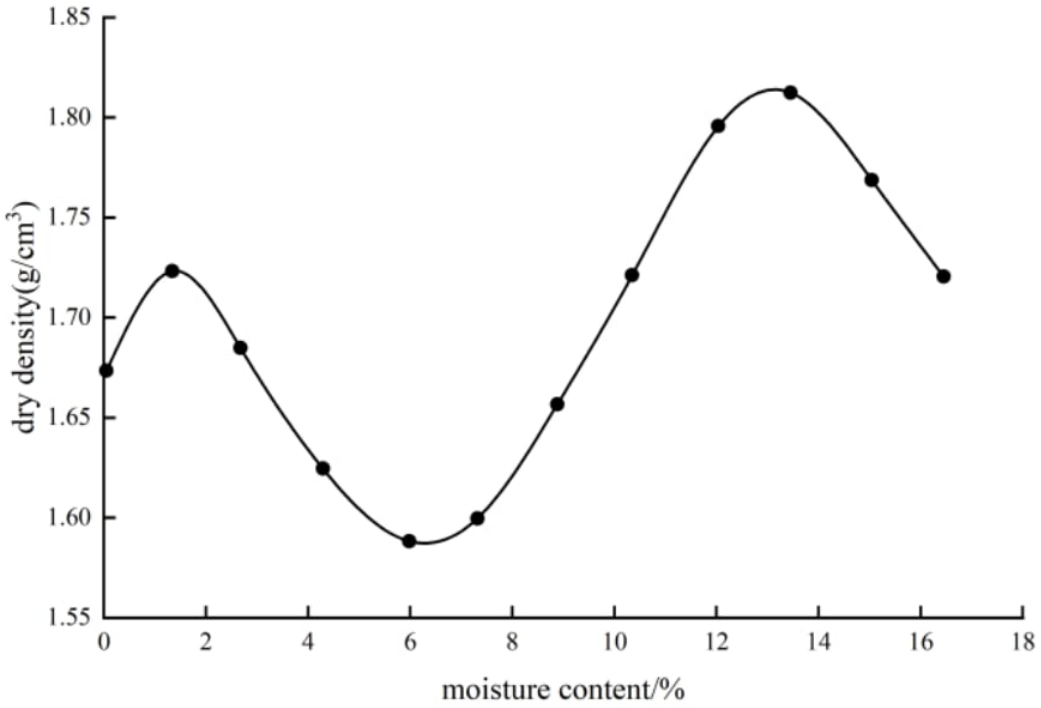

Figure 2. Compaction curve of aeolian sand.

As shown in the above figure, the dry density of the aeolian fine sand test specimens shows a bimodal variation with increasing moisture content. At a moisture content of 0%, the dry density is 1.67 g/cm^3. When the moisture content reaches 1.33%, the dry density reaches the first peak of 1.723 g/cm^3. With increasing moisture content, the dry density gradually decreases, reaching a minimum at a moisture content of 6.29%. When the moisture content increases to 13.45%, the dry density reaches the second peak of 1.812 g/cm^3. Subsequently, the dry density gradually decreases with increasing moisture content. This phenomenon is consistent with the findings of Al-Sanad HA et al. [30,31]. The reason the compaction curve for aeolian sand exhibits two peaks is that this material can achieve high compaction densities both in dry and saturated states—a characteristic property of aeolian sand compaction. At the first peak, the sand is highly loose with negligible cohesion, and compaction primarily overcomes internal friction, thus readily attaining its maximum dry density in its natural state [32]. Under the arid conditions of deserts, moisture levels rarely attain the second peak moisture content. Consequently, compacting aeolian sand at the second peak is economically impractical. Given that aeolian sand can be compacted in its dry state, the optimum moisture content and maximum dry density represented by the first peak are selected as the foundation for subsequent studies to align with practical engineering conditions.

To study the mechanical properties of aeolian sand, triaxial shear tests were conducted on the aeolian sand. The main aim of the experiment was to study the peak deviatoric stress of aeolian sand under confining pressures of 50 kPa, 100 kPa, 150 kPa, 200 kPa, 300 kPa, and 500 kPa using the DJSZ-150 large triaxial testing machine of the Institute of Rock and Soil Mechanics, Chinese Academy of Sciences, in Wuhan, China. The samples were cylindrical, with a diameter of 300 mm and a height of 600 mm, and the test process is shown in Figure 3.

For the triaxial tests, the specimens were prepared at a moisture content of 0% and a compaction degree of 97%. Each specimen was compacted in six successive layers, with a thickness of approximately 100 mm per layer. Three specimens were tested under each confining pressure, resulting in 18 triaxial specimens in total.

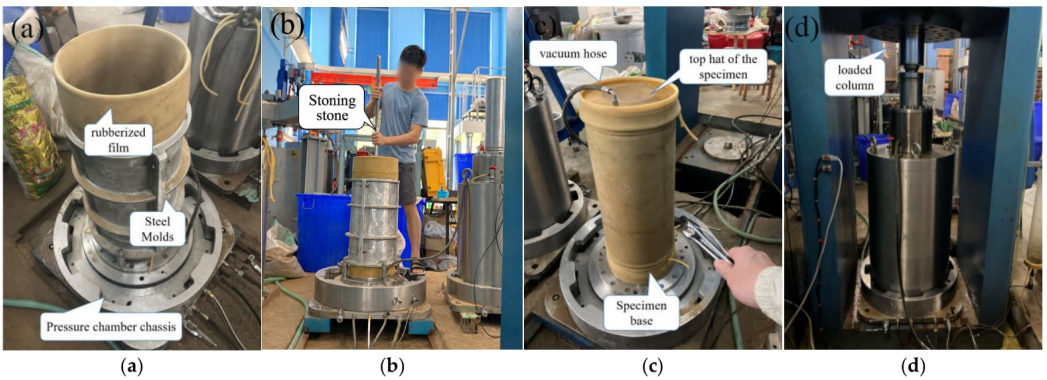

Figure 3. Triaxial test process for aeolian sand. (**a**) Rubber film and mold installation. (**b**) Dense vibration. (**c**) Complete sample preparation. (**d**) Loading.

According to the experimental results, a graph of the deviatoric stress vs. axial strain relationship was plotted, as shown in Figure 4. It was observed from the graph that the deviatoric stress of aeolian sand changes with axial strain in three stages. In the first stage, the stress–strain relationship is linear, indicating that elastic deformation is the dominant behavior of the aeolian sand in this stage. As the axial strain increases, the relationship between stress and strain enters the second stage, showing nonlinearity, indicating the plastic deformation stage, and a peak deviatoric stress can be observed in this stage. In the third stage, the stress shows a decreasing trend overall, but the strain increases rapidly, indicating a rapid plastic deformation stage and strain softening behavior of the specimen. Additionally, at different confining pressures, significant differences in the stress–strain relationships are observed. With increasing confining pressure, the rate of increase in axial stress increases, and the peak deviatoric stress and residual strength also increase significantly. This is mainly because with increasing confining pressure, the soil is compacted more tightly, and both the modulus and shear strength of the soil are significantly increased, resulting in a significant increase in the slope, peak strength, and residual strength of the deviatoric stress–strain curve.

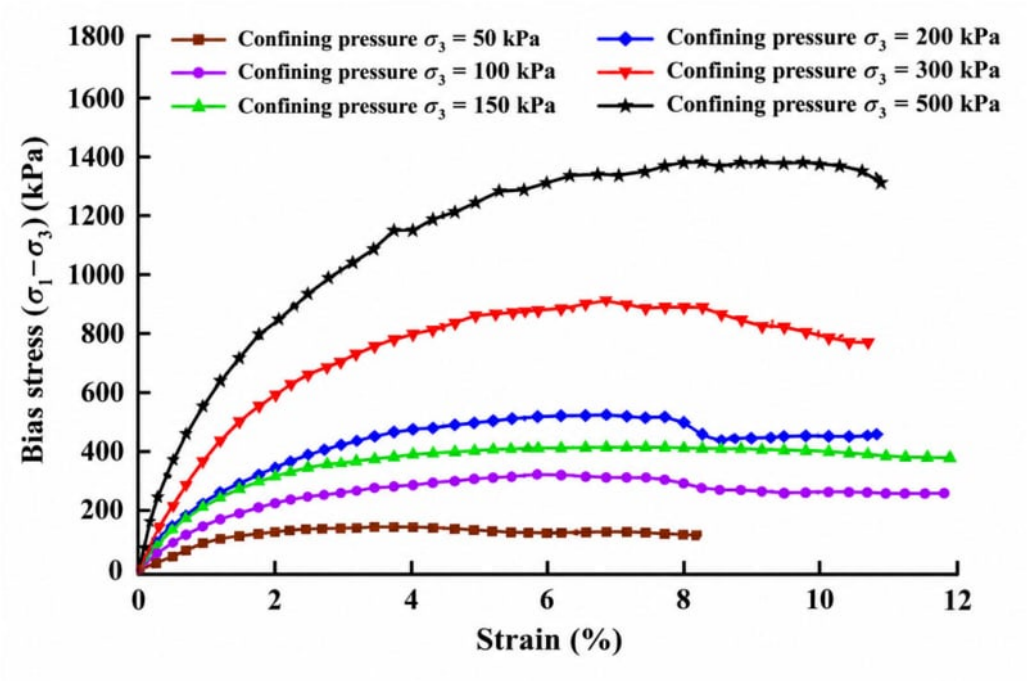

Figure 4. Stress–strain curves of aeolian sand.

According to the stress–strain curve above, the peak deviatoric stress was used as the criterion for strength failure, and the deviatoric stresses of the specimens at failure under different confining pressures were extracted, as detailed in Table 2. The normal stress was used as the horizontal axis, and the shear stress was used as the vertical axis to plot the Mohr stress circle at failure. There are a total of 6 confining pressure conditions in the experiment, resulting in 6 Mohr stress cycles. By drawing tangent lines to these Mohr circles, the strength envelope of the aeolian sand is obtained, as shown in Figure 5. Further calculation of the strength envelope yields an internal friction angle φ of 36.1° and cohesion c of 1.5 kPa for aeolian sand.

Table 2. Peak deviatoric stress at each confining pressure.

Stresses/kPa	Confining Pressure σ_3/kPa					
	50	100	150	200	300	500
Breaking deviatoric stress σ_1–σ_3	157	331	409	527	900	1434

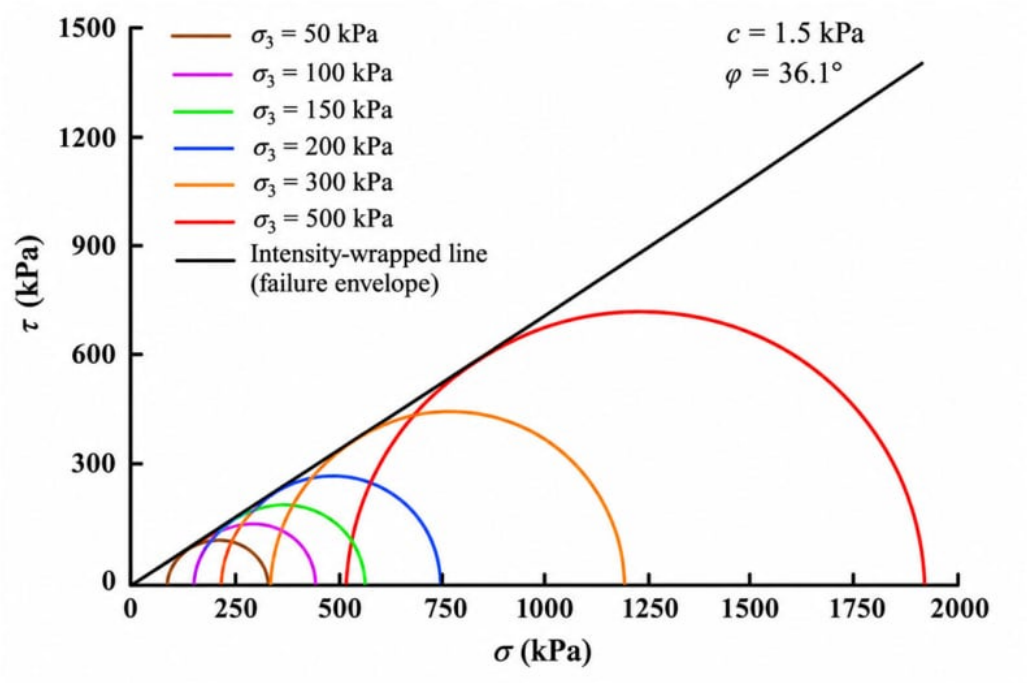

Figure 5. Mohr's circle and strength envelope of aeolian sand.

The aeolian sand was modeled using a Mohr–Coulomb elastoplastic constitutive model rather than a purely linear-elastic formulation. The shear-strength parameters were determined directly from the triaxial test results. Specifically, the peak deviator stresses measured under confining pressures of 50, 100, 150, 200, 300, and 500 kPa were used to construct the corresponding Mohr circles and establish the Mohr–Coulomb failure envelope. Based on this analysis, the internal friction angle and cohesion were determined to be 36.1° and 1.5 kPa, respectively. Poisson's ratio was calculated to be 0.29 from the at-rest earth pressure coefficient estimated using the internal friction angle. An elastic modulus of 35 MPa was assigned to characterize the pre-yield elastic response of the aeolian sand. No additional hardening law was incorporated; consequently, the post-yield behavior was governed by the conventional ideal elastoplastic Mohr–Coulomb formulation.

Because no independent unloading–reloading triaxial tests were available, the unloading and reloading response was represented using the same elastic parameters (E = 35 MPa

and $\nu = 0.29$) within the adopted Mohr–Coulomb constitutive model, without introducing a separately calibrated unloading modulus.

In addition, according to soil mechanics, aeolian sand in a semiinfinite foundation is under lateral confining stress [33,34]. The lateral earth pressure coefficient K0 of aeolian sand can be calculated according to the following formula based on the internal friction angle:

$$K_0 = 1 - \sin\varphi \quad (1)$$

The general Hooke's law suggests that

$$K_0 = \frac{\nu}{1-\nu} \quad (2)$$

By simultaneously solving Equations (1) and (2), we can obtain the following formula for Poisson's ratio ν:

$$\nu = \frac{K_0}{1+K_0} = \frac{1-\sin\varphi}{2-\sin\varphi} \quad (3)$$

According to Equations (2) and (3), the static earth pressure coefficient K0 of the aeolian sand is calculated to be 0.41, with a Poisson's ratio ν of 0.29.

2.1.2. Geocell Specimen

The geocell used in the reinforced aeolian-sand subgrade is made of high-density polyethylene (HDPE). The representative geocell unit adopted in the numerical model has dimensions of 400 mm × 400 mm × 150 mm (length × width × height), with a sheet thickness of 0.57 mm. Its geometric configuration and dimensions are illustrated in Figure 6.

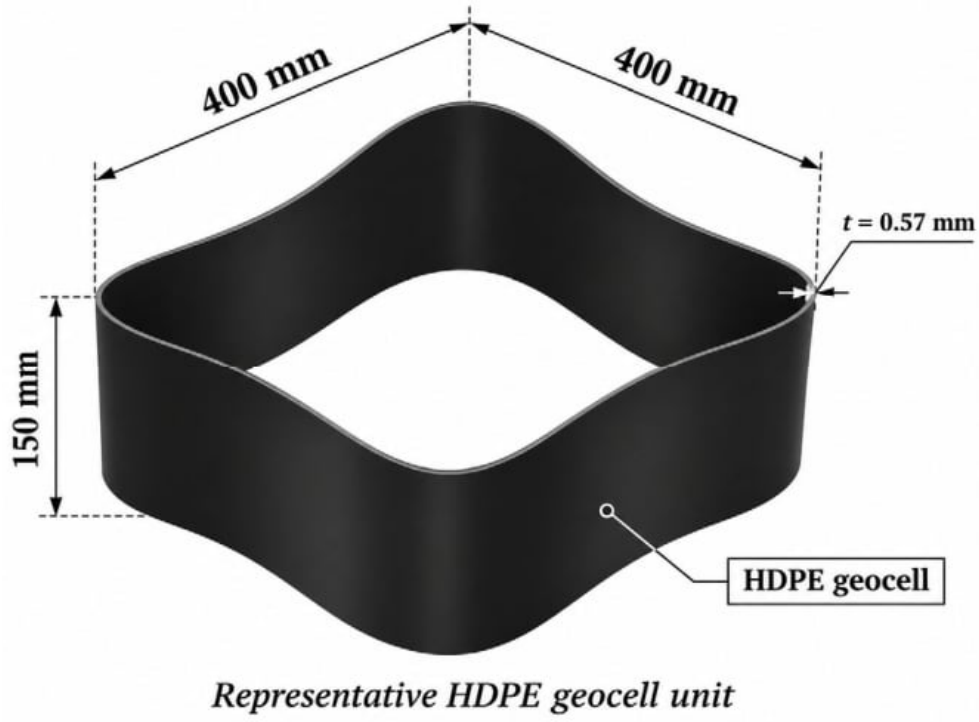

Figure 6. Three-dimensional schematic of the HDPE geocell unit and its geometric dimensions.

2.2. Field Test

2.2.1. Subsubsection

To verify the reliability of the above model, a field test was conducted on the newly constructed S21 Desert Highway. The test section selected was from K233 + 600 to K233 + 750 in the desert area. The highway adopts a two-way four-lane separated embankment, with

contrasting schemes set on the left and right sides. The left side is the original design with gravel-type soil as the roadbed (Scheme 1), and the right panel shows a geocell-reinforced windlogged sand new roadbed (Scheme 2). To study the dynamic characteristics of the embankment and the reinforcement effect of the geocells, 4 sets of dynamic soil pressure boxes were buried in the embankment below the centerline of the road surface on both the left and right sides, as shown in Figure 7. A JMYJ-1410 resistive strain-type dynamic soil pressure box was used as the testing sensor, with a measuring range of ±10,000 με. The data acquisition unit used was the JMYD-1008 8-channel signal acquisition instrument, with an adjustable frequency range of 5 Hz to 200 Hz. In this experiment, considering the accuracy of data acquisition and the amount of data collected, a sampling frequency of 100 Hz was used for the vibration soil pressure data collection. The sampling frequency of 100 Hz corresponds to a Nyquist frequency of 50 Hz. However, the sampling frequency alone does not characterize the frequency response or effective measurement bandwidth of the complete sensor–acquisition system. The 8-channel signal acquisition instrument used in the experiment is shown in Figure 8.

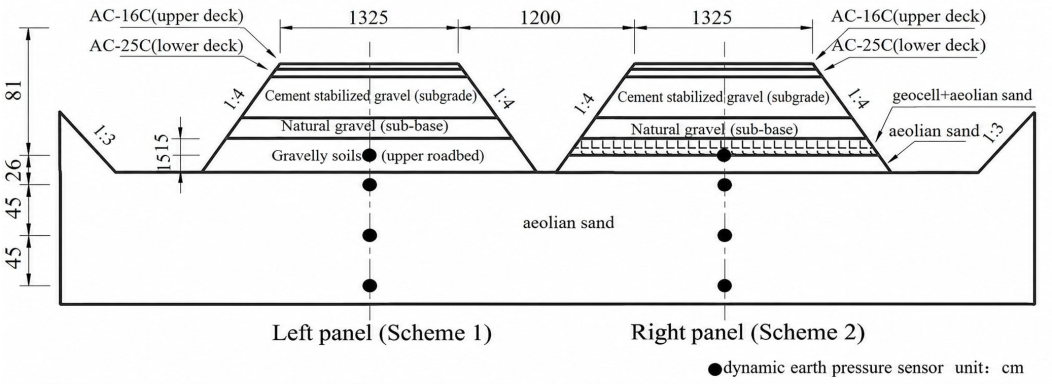

Figure 7. The structure of the highway cross-section and the layout of the dynamic earth pressure sensors.

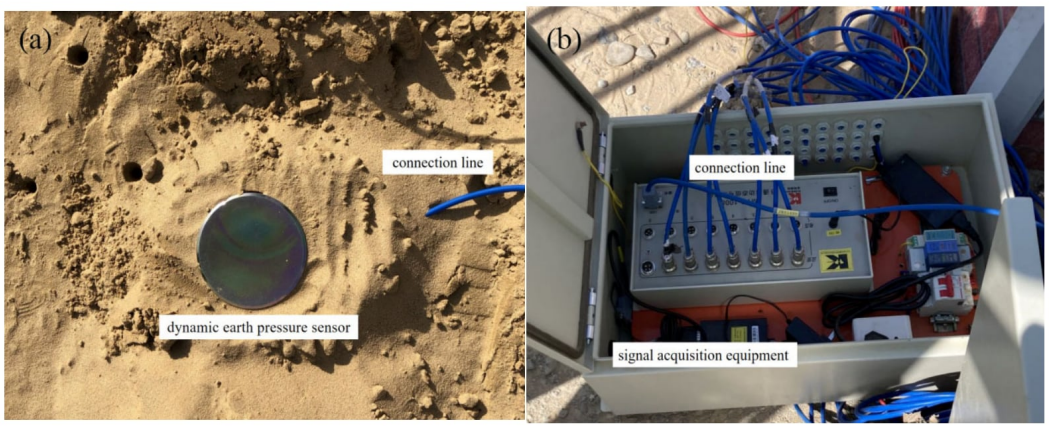

(**a**) Dynamic soil stress signal (**b**) Acquisition equipment for field tests

Figure 8. Dynamic soil stress signal acquisition equipment for field tests.

The conventional gravel–soil roadbed was selected as the reference configuration because it represents the conventional roadbed construction scheme adopted for the S21 Desert Highway project. By contrast, the geocell-reinforced aeolian sand roadbed was considered an alternative configuration that utilizes locally available aeolian sand. Accordingly, the comparison between Scheme 1 and Scheme 2 was designed to evaluate the overall dynamic

performance of these two engineering configurations, rather than to isolate and quantify the contribution of geocell reinforcement alone.

2.2.2. Test Scheme

To study the dynamic characteristics of roadbed structures under different vehicle operating conditions and the reinforcement effect of geogrid chambers, the road base compaction control was set to 97% and the optimal moisture contents of the aeolian sand and gravel soil were adopted. When vehicles passed through the test section, it was necessary to ensure that the trajectory line of the vehicle passed directly above the buried dynamic soil pressure box. Therefore, during the test, the trajectory line passing through the dynamic soil pressure box was drawn on the road surface in advance. Then, the truck was loaded with the base material in the material yard, the total weight of the vehicle and material was checked on the weighbridge, and the vehicle was driven to the test section after reaching the preset weight. A cone bucket was used to guide the driver's line of sight to ensure that the vehicle followed the trajectory line drawn in advance. To ensure that the vehicle reached the predetermined speed when passing through the test section, a sufficient acceleration length was reserved in the test. The truck model used in the test was a Shaanqi SX 3256DR3841, with a total mass of 43 t after loading. Four dynamic earth-pressure sensors were installed beneath the pavement centerline for each roadbed scheme, resulting in eight monitoring locations in total. The sensors were vertically arranged at approximately 0.81, 0.96, 1.41, and 1.86 m below the pavement surface, as shown in Figure 7. Dynamic stress signals were recorded at a sampling frequency of 100 Hz. For each vehicle-speed condition, the 43 t test truck passed through the monitoring Section 4 times along the prescribed wheel path, and the repeated measurements were used to evaluate the consistency of the field response. The field driving tests were conducted on two roadbed configurations: the conventional gravel–soil roadbed (Scheme 1) on the left section and the geocell-reinforced aeolian sand roadbed (Scheme 2) on the right section. The same test vehicle, with a total mass of 43 t, was used for both configurations. To distinguish the effects of roadbed structure and vehicle speed, driving tests were conducted at 20 and 60 km/h on each roadbed configuration. Thus, both roadbed configurations were evaluated under identical vehicle mass and speed conditions, allowing direct comparisons of their dynamic stress responses.

The detailed field driving test matrix for the two roadbed configurations is presented in Table 3.

Table 3. Field driving test matrix for the two roadbed configurations.

Roadbed Configuration	Vehicle Mass (t)	Vehicle Speed (km/h)	Repetitions
Scheme 1: Gravel–soil roadbed	43	20	4
Scheme 1: Gravel–soil roadbed	43	60	4
Scheme 2: Geocell-reinforced aeolian sand roadbed	43	20	4
Scheme 2: Geocell-reinforced aeolian sand roadbed	43	60	4

The field driving test site, test vehicle, and test section are shown in Figure 9.

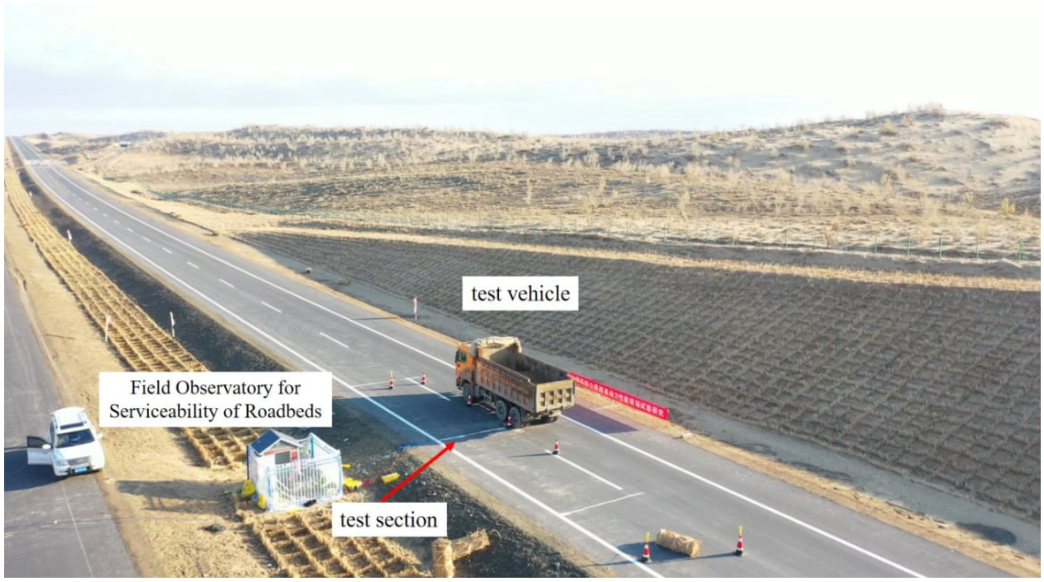

Figure 9. Field tests with moving vehicles.

2.3. Numerical Modeling

During vehicle operation, the contact between the tires and the road surface causes vibrations in the roadbed. These vibrations, in turn, affect the wheels and the vehicle body, forming a dynamic coupling system between the vehicle body, wheels, and the road. The mechanical performance of the wheels, as the direct interface between the vehicle and the road surface, directly affects the vibration effects of the vehicle on the road. In many finite element analyses, researchers simplify the modeling of wheels by considering them multiple moving loads due to the complexity and computational resources required for tire modeling. By establishing a complete vehicle model and considering the superposition effect of tire vibrations, the dynamic characteristics of a reinforced soil roadbed under vehicle loading can be analyzed.

2.3.1. Vehicle Structure

The vehicle prototype is a Shaanxi Automobile SX3256DR3841 truck, which is a three-axle ten-wheel truck. It adopts a "single steering axle + double drive axle" structure, with single tires on each side of the front axle and double tires on each side of the middle and rear axles. The structural parameters of the vehicle and the complete vehicle model are shown in Figure 10.

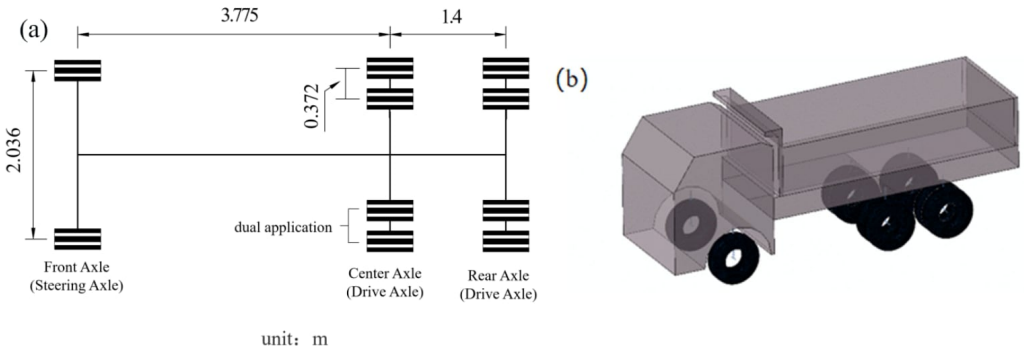

(**a**) Structure of Shaanxi Automobile SX3256DR3841 Vehicle (**b**) Vehicle finite element model structure

Figure 10. Vehicle structure diagram.

Body Model

The modulus of the vehicle body is much greater than that of the tires, so the body is assumed to be completely rigid and modeled as a discrete rigid body to form a load-bearing body. Discrete rigid body modeling is suitable for cases where element deformation can be ignored. Its advantage over deformable body modeling is that rigid body modeling can considerably reduce computations. However, discrete rigid bodies cannot have material mass properties. Therefore, mass reference points are set on the discrete rigid bodies to simulate the inertia and weight of the entire vehicle.

The rigid-body approximation was adopted to reduce computational cost while retaining the overall mass and inertial response of the vehicle. This simplification neglects local deformation and structural vibration of the truck frame. Nevertheless, the vertical motion of the vehicle body and the load transfer through the suspension system are represented by the connector elements. Therefore, the model is intended to reproduce the overall vehicle-induced loading response rather than the detailed structural vibration of the truck body.

The body is connected to the wheels through suspension and axles, and the interaction between the suspension and axles is simulated using ABAQUS connector elements. Different connector properties can be used to describe relative motion constraints such as translation and rotation. In addition, different connector behaviors can be used to describe interactions such as elasticity, plasticity, damping, friction, locking, damage, and failure. In the model, the translator property of the connector element is used to provide vertical degrees of freedom between the body and a wheel axle. The elastic and damping connector behaviors are also set in parallel to simulate the vertical support and energy dissipation functions of the suspension. The specific parameters of the suspension are shown in Table 4. The hinge property of the connector element is used to simulate the wheel axle, providing relative rotational degrees of freedom between the body and the wheels. The assembly structure of the translator and hinge connector properties of the vehicle model is shown in Figure 11. During vehicle operation, these two types of interactions form a dynamic transmission system that combines wheel rolling and vertical vibration of the body.

Table 4. Suspension parameters.

Parameters	Suspension Stiffness/kN.m^{-1}	Friction/kN.s.m^{-1}
front suspension	300	10
center suspension	800	25
rear suspension	800	25

The vehicle model is based on the Shaanxi Automobile SX3256DR3841 three-axle lorry used in on-site driving tests; a dynamic model of the body–suspension–tire system was established based on the vehicle's structure and the on-site test conditions. The body is represented as a discrete rigid body, whilst the suspension is simulated using connection elements that exhibit vertical translation, elastic support and damping behavior. Table 4 lists the equivalent vertical stiffness and damping coefficients for the front, center and rear suspensions.

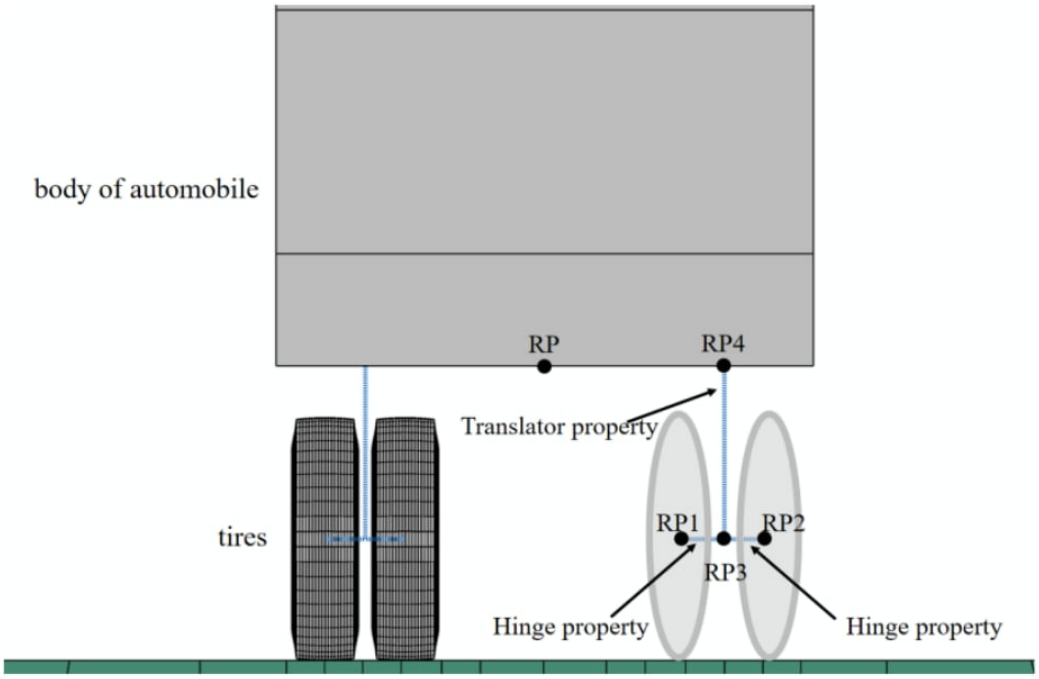

Figure 11. Vehicle assembly structure.

Tire Model

The conventional modeling method for numerical models of tires involves defining the carcass ply on the surface elements of different structural layers by setting reinforcements and then embedding the surface elements and bead wire elements into the corresponding rubber matrix elements. However, this method has drawbacks such as many elements and a complex modeling process. To simplify tire modeling and calculation, the following modeling method is proposed: First, all rubber structural layers of the tire are merged, and a hard triangular rubber with strong shear resistance is used as the rubber matrix material of the tire. The surface elements of the various structural layers of the tire are removed; instead, the skin is set on the inner surface of the tire, and the carcass ply is set on the skin. The specific modeling process is as follows:

First, the tire contour DXF file is imported into HyperMesh software 2020 and divided into a 2D plane mesh. Then, the mesh is rotated and duplicated to generate three-dimensional solid tire elements. The generated solid elements are imported into ABAQUS. One skin, skin1, is set on the inner surface of the tire in the projection area of the tread. Another skin, skin2, is set on the entire inner surface. The skins are shown in Figure 12. On skin1, four layers of reinforced ply with cord layers are set. On skin2, the carcass ply reinforcement is set. Additionally, to enhance the overall stiffness, two carcass reinforcements, rebar1 and rebar2, are added to skin2. The structure of the reinforcements is set such that the cord spacing is 0.0205 m, and the angles to the meridian plane are 70° and −70°. The other parameters are the same as those of the carcass reinforcement. The tire bead and the reference point of the wheel center are constrained as a rigid body, representing the fixed contact between the wheel rim and the tire. Since there are overlapping nodes between the rigid body constraint region of the bead and skin2, the bead wire of the conventional tire model, which fixes the carcass ply, and the bead wire of the bead package are removed.

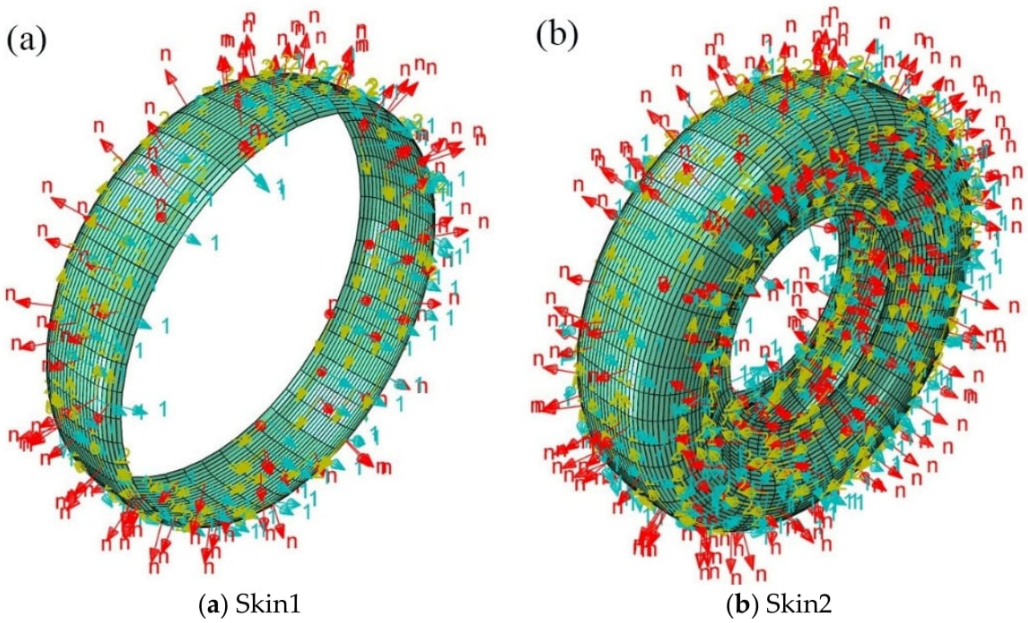

Figure 12. Model of tire skin.

To verify the feasibility of the tire model, the radial stiffness of the tire model is compared with the empirical formula for radial stiffness. After inflating the tire model, a series of vertical loads are applied to the wheel center position, and the load and vertical displacement of the wheel center are collected during the loading process. The contour plot of the vertical displacement of the tire after applying the wheel center load is shown in Figure 13.

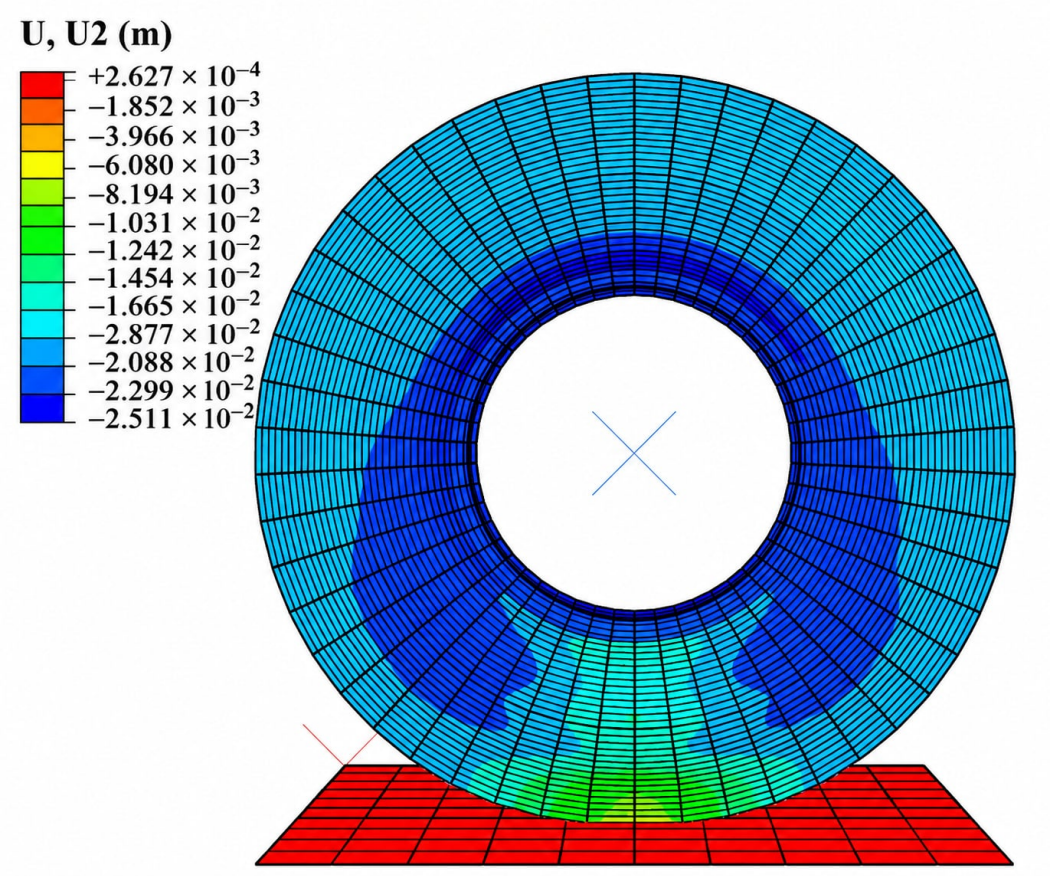

Figure 13. Contour diagram of tire displacement under axle load.

The empirical formula for the relationship between the load and wheel center deflection is as follows [35,36]:

$$\delta = c\frac{W^{0.85}}{B^{0.7}D^{0.43}p^{0.6}}K \tag{4}$$

$$K = 15 \times 10^{-3} \times B + 0.42 \tag{5}$$

In Equations (4) and (5), δ represents the wheel center deflection (cm) and c is a parameter related to the tire structure design. For radial tires, $c = 1.5$, and for bias-ply tires, $c = 1.15$. W represents the wheel center load (10 N), and B represents the tire width (cm). For a 12.00R20 tire, B is taken as 30.48 cm, D represents the tire diameter (cm), which is taken as 112.5 cm, and p represents the tire inflation pressure (kPa), which is taken as 830 kPa.

Figure 14 shows the curve of the relationship between the load and wheel center deflection. From the graph, it can be observed that the maximum deviation between the empirical formula and the calculated values from the model is 4.710%. This indicates that the results of the tire model are in good agreement with the mechanical characteristics of the actual tire, demonstrating that this modeling method is accurate and effective.

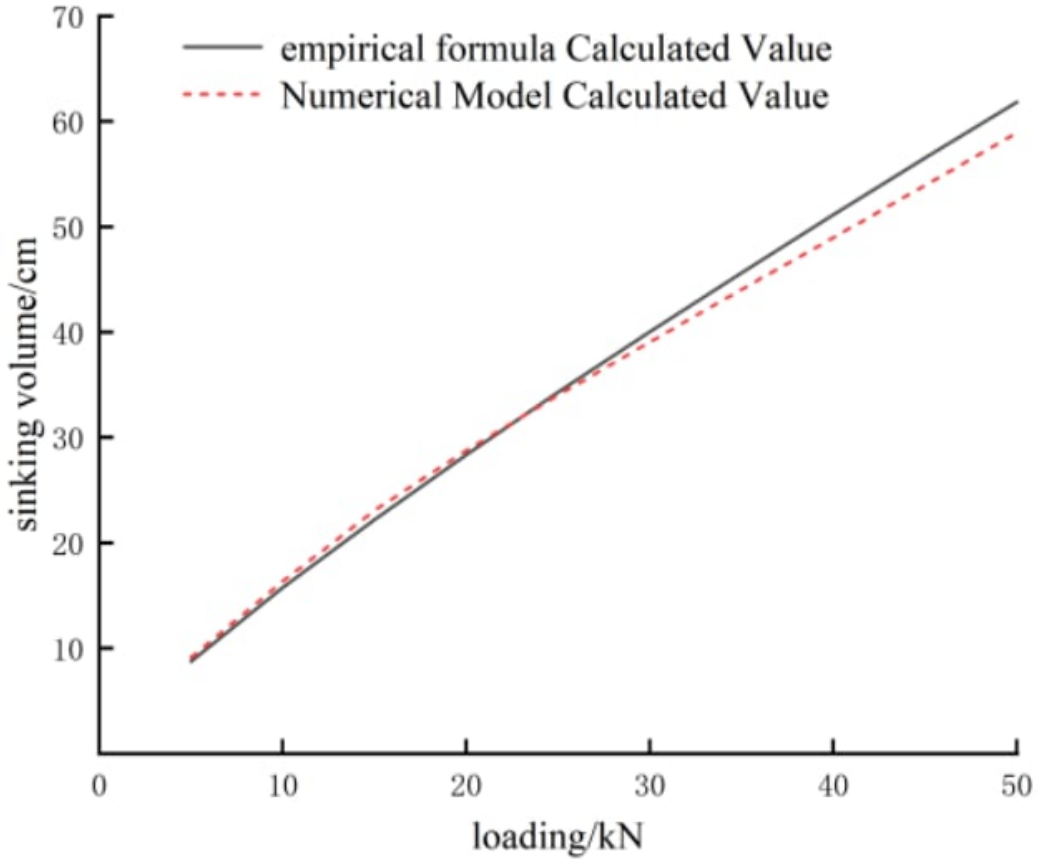

Figure 14. Load–sinkage curve of tire.

To further investigate the computational cost of the tire model established using the new method, a complete tire model is built using the conventional method. The inflation calculation is performed on the tire models constructed using both methods. The time taken for the inflation calculation using the conventional method (Method 1) and the method proposed in this paper (Method 2) is shown in Figure 15. According to the graph, when using the ABAQUS/Standard algorithm, the computation time of Method 2 is 7.98% of that of Method 1. When using the ABAQUS/Explicit algorithm, the computation time of

Method 2 is 2.38% that of Method 1. This indicates that the tire model constructed using the new method has a significant advantage in reducing computational costs compared to the conventional method. This advantage is due to two reasons. First, the face elements containing the ply steel cord of the belt layer, the carcass steel cord, and the bead steel cord are removed and replaced with two layers of skin, which reduces the number of elements. Second, the algorithm for the skin is different from that for the face elements, which require a separate algorithm for the high-computational constraint between the rubber matrix and the elements. This reduces the number of equations to be solved. Additionally, the skin does not require separate meshing, as do the face elements, thereby reducing the complexity of tire modeling compared to traditional methods.

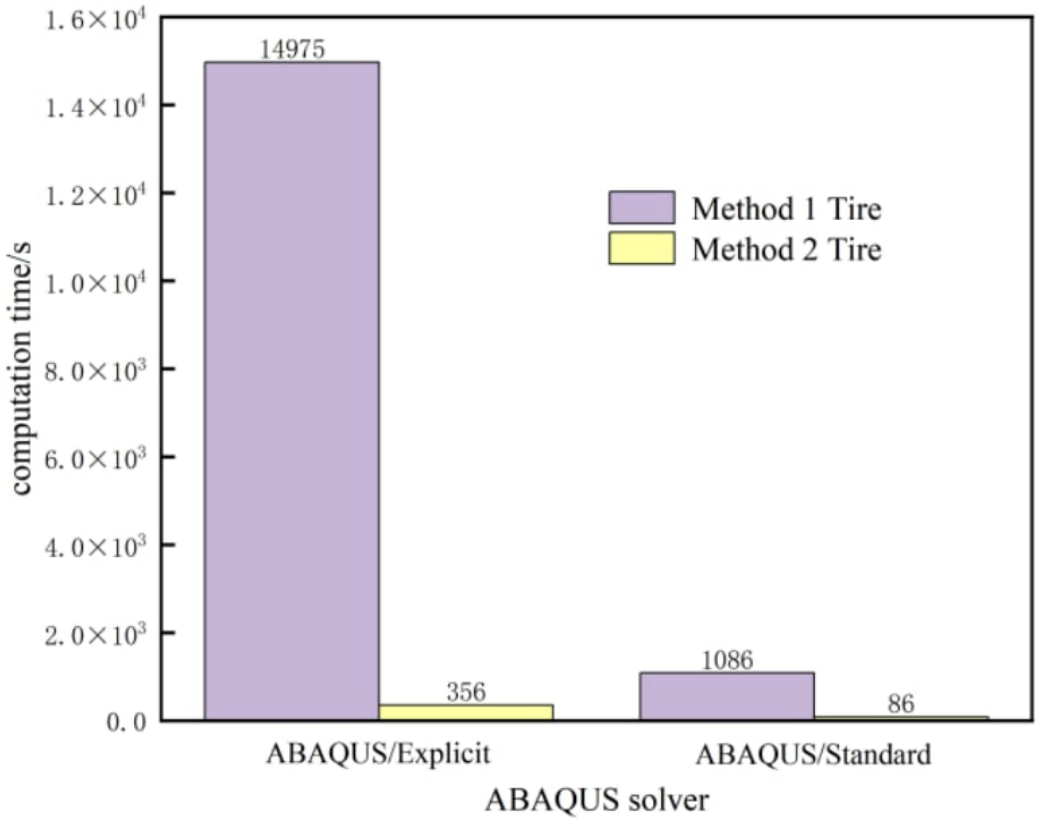

Figure 15. Comparison of the calculation times for tire models established via two methods.

2.3.2. Highway Model

When analyzing the model, certain parts require special attention, so the mesh division of these parts should be as fine as possible to ensure more accurate finite element calculation results. The less critical parts can be divided with a coarser mesh to reduce the number of elements. Transitional meshes are needed between fine and coarse meshes, which are mainly divided into two types, 1:2 type and 1:3 type, as shown in Figure 16.

To evaluate the sensitivity of the numerical results to the spatial discretization, three local mesh sizes of 100, 75, and 50 mm were examined, corresponding to the coarse, medium, and fine mesh schemes, respectively. The peak stress and attenuation coefficient were selected as the comparison indices. The results of the mesh sensitivity analysis are summarized in Table 5.

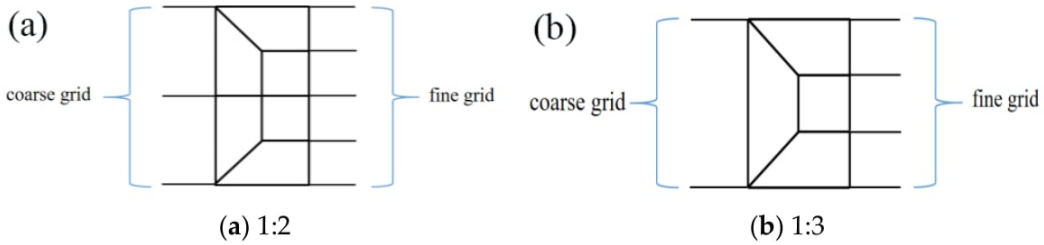

Figure 16. Schematic diagram of the transitional mesh.

Table 5. Mesh sensitivity analysis of the highway finite element model.

Mesh	Local Element Size	Peak Stress (kPa)	Attenuation Coefficient
Coarse	100	13.65	0.594
Medium	75	13.22	0.582
Fine	50	13.16	0.58

As shown in Table 5, mesh refinement from 100 to 75 mm produces an evident change in the calculated response, whereas further refinement from 75 to 50 mm results in only a small variation. Specifically, the peak stress changes from 13.22 to 13.16 kPa, corresponding to a difference of approximately 0.46%, while the attenuation coefficient changes from 0.582 to 0.580, with a difference of approximately 0.34%. These results indicate that the numerical response has essentially converged at the medium mesh level. Therefore, a local element size of 75 mm was adopted in the subsequent simulations to provide an appropriate balance between numerical accuracy and computational efficiency.

In addition to the mesh sensitivity analysis, the influence of the time increment in the ABAQUS/Explicit analysis was examined. Three time increments, namely 1.10×10^{-6}, 5.50×10^{-7}, and 2.75×10^{-7} s, were compared using the same peak-stress and attenuation-coefficient indices, as summarized in Table 6.

Table 6. Time-increment sensitivity analysis of the ABAQUS/Explicit model.

Case	Time Increment	Peak Stress (kPa)	Attenuation Coefficient
T1	1.10×10^{-6}	13.24	0.582
T2	5.50×10^{-7}	13.17	0.579
T3	2.75×10^{-7}	13.15	0.577

As the time increment decreases, both response quantities gradually approach stable values. In particular, reducing the time increment from 5.50×10^{-7} s to 2.75×10^{-7} s changes the peak stress from 13.17 to 13.15 kPa, corresponding to approximately 0.15%, while the attenuation coefficient changes from 0.579 to 0.577, corresponding to approximately 0.35%. The limited variation indicates that further reduction in the time increment has only a minor influence on the calculated response. Therefore, a time increment of 5.50×10^{-7} s was adopted in the subsequent analyses as a compromise between numerical accuracy and computational efficiency.

The area beneath the tire tracks is the focus of this article, so a refined grid is used in this region. A coarse grid is used in areas away from the tire tracks. A 1:3 transitional grid is employed to facilitate a quick transition between grids of different sizes. The approach to creating a transitional grid in ABAQUS involves initially drawing the transitional grid of the road surface using AutoCAD 2019. This grid is then imported into ABAQUS as a sketch, and the sketch is used to cut the upper surface of the road components. Each edge

is assigned a single element seed, and the constraint is set to prevent changing the number of elements. Finally, the sweep method is used as the meshing technique, and the sweeping path is redefined to be downward along the depth of the road, thereby achieving meshing of the transitional grid.

To study the reinforcement effect of geocells on subgrades, two highway models were established based on the Xinjiang S21 Desert Highway project: a conventional gravel subgrade model (Scheme 1) and a geocell-reinforced aeolian sand subgrade model (Scheme 2). The gravel subgrade model has a length of 30 m, a roadbed width of 12.35 m, a height of 0.96 m, and a foundation height of 5 m. The cross-sectional structure of the roadbed is as follows: 0.12 m surface layer, 0.36 m base layer, 0.18 m subbase layer, and 0.30 m gravel subgrade. The geocell-reinforced aeolian sand subgrade model is based on the gravel subgrade model, with the 0.3 m thick gravel layer replaced by a 0.15 m geocell-reinforced aeolian sand layer and 0.15 m pure aeolian sand layer. Infinite elements can absorb the energy transferred from adjacent finite elements. To avoid wave reflection at the free boundary, infinite elements are set around the highway model and at the bottom to simulate the far boundary of the subgrade. The finite element mesh model of the highway is shown in Figure 17, and the material parameters of each structural layer are shown in Table 4. The material parameter values for the pavement structure (surface layer, base layer, subbase layer) in this table are primarily referenced from highway finite element models by Zhao [37], Wang [38], and others. The material parameter values for gravel soil are mainly referenced from experimental results by Zhou [39], Cai [40], Liu [41] and others. The material parameter values for the geocells are based on the strip tensile test results obtained by Ma [42] and others.

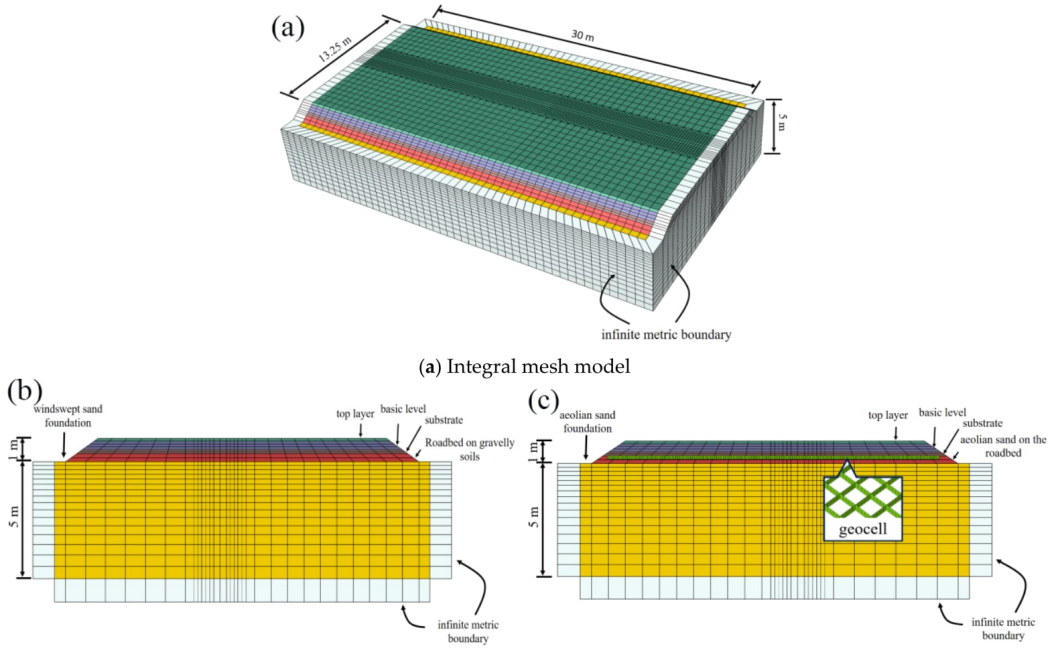

(**a**) Integral mesh model

(**b**) Scheme 1 grid model

(**c**) Scheme 2 grid model

Figure 17. Finite element mesh of highway model.

A single geocell has dimensions of 400 mm × 400 mm × 150 mm (length × width × height), with a thickness of 0.57 mm for each geocell sheet. The geocell sheets are simulated using membrane elements, which only transmit forces within the plane and provide strength while neglecting the bending stiffness in the thickness direction. This simulation captures the high tensile modulus, high tensile strength, and low bending stiffness characteristics of the geocell sheets.

The geocell was represented using linear elastic membrane elements with an elastic modulus of 1050 MPa, as specified in Table 4. This simplified representation was adopted to describe the in-plane tensile response of the geocell under transient vehicle loading while neglecting its bending stiffness. The membrane formulation allows the geocell to undergo in-plane elastic deformation and displacement. However, the linear elastic assumption does not account for the nonlinear, viscoelastic, or time-dependent behavior of HDPE, which may become important under large deformation or repeated loading.

The geocell elements are embedded into the corresponding solid elements of the subgrade using the *EMBEDDED ELEMENT command. The translational degrees of freedom of the geocell element nodes are eliminated by interpolating the degrees of freedom of the subgrade solid element nodes, while the geocell elements with higher moduli restrict the deformation of the aeolian sand subgrade elements. This interaction demonstrates the reinforcing effect of the geocell on the subgrade.

The embedded-element constraint was adopted to represent an idealized interaction between the geocell and the surrounding aeolian sand. Under this constraint, the translational motion of the geocell nodes follows the interpolated displacement field of the host soil elements. Therefore, the geocell can undergo elastic deformation and move together with the surrounding soil, but relative sliding and separation at the geocell–sand interface are not explicitly represented. This assumption simplifies the numerical treatment of the reinforcement–soil interaction but may overestimate the degree of interfacial load transfer compared with conditions where relative slip occurs.

The constitutive models and material parameters used for the pavement and roadbed are summarized in Table 7. In particular, the aeolian sand and gravelly soil were modeled using the Mohr–Coulomb elastoplastic model.

Table 7. Highway material parameters.

Materials	Isomorphic Model	Elastic Modulus/MPa	Poisson's Ratio	Density kg/m^3	Damping Ratio	Internal Friction Angle/°	Cohesive Force/kPa
top layer	linear elasticity	1300	0.35	2500	0.01	-	-
base level	linear elasticity	800	0.25	2400	0.02	-	-
substrate	linear elasticity	600	0.25	2200	0.02	-	-
gravelly soil	Mohr–Coulomb	100	0.27	2120	0.09	39	15
aeolian sand	Mohr–Coulomb	35	0.29	1620	0.05	36.1	1.5
geocell	linear elasticity	1050	0.25	950	-	-	-

2.4. Model Validation Method

Figures 18 and 19 show the time history curves of the measured data and their smoothed values obtained from field tests and numerical model calculations. From the figures, it can be observed that the stress values of both the field measurements and numerical calculations oscillate up and down along a certain trend over time. The oscillations in the field measurements may be related to the equipment itself, noise in the current, and vibrations caused by vehicle movement on the highway. The oscillations in the numerical calculations are mainly caused by the vibrations induced by vehicle movement. Directly comparing the raw signal values can be challenging, so it is necessary to remove these unwanted oscillations through smoothing before analyzing the response. In this study, smoothing techniques were employed to remove signal oscillations, and the resulting trend lines were used to represent the corresponding dynamic stress–time history curves. Fast Fourier transform (FFT) smoothing was used to improve the signal-to-noise ratio of the raw signals [43], and different FFT smoothing iterations were applied to the raw data obtained

from different methods. Considering the smoothness of the trend lines, 10 iterations of smoothing were applied to the field measurements, while 6 iterations were applied to the simulated measurements.

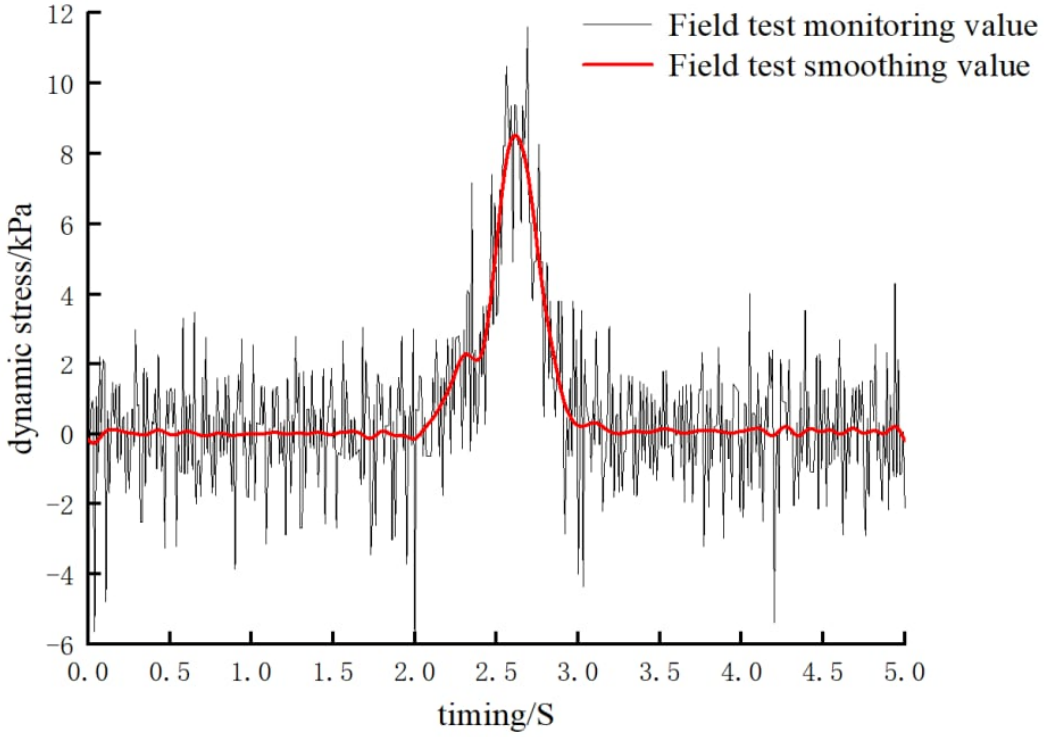

Figure 18. Field-measured dynamic stress–time history curves.

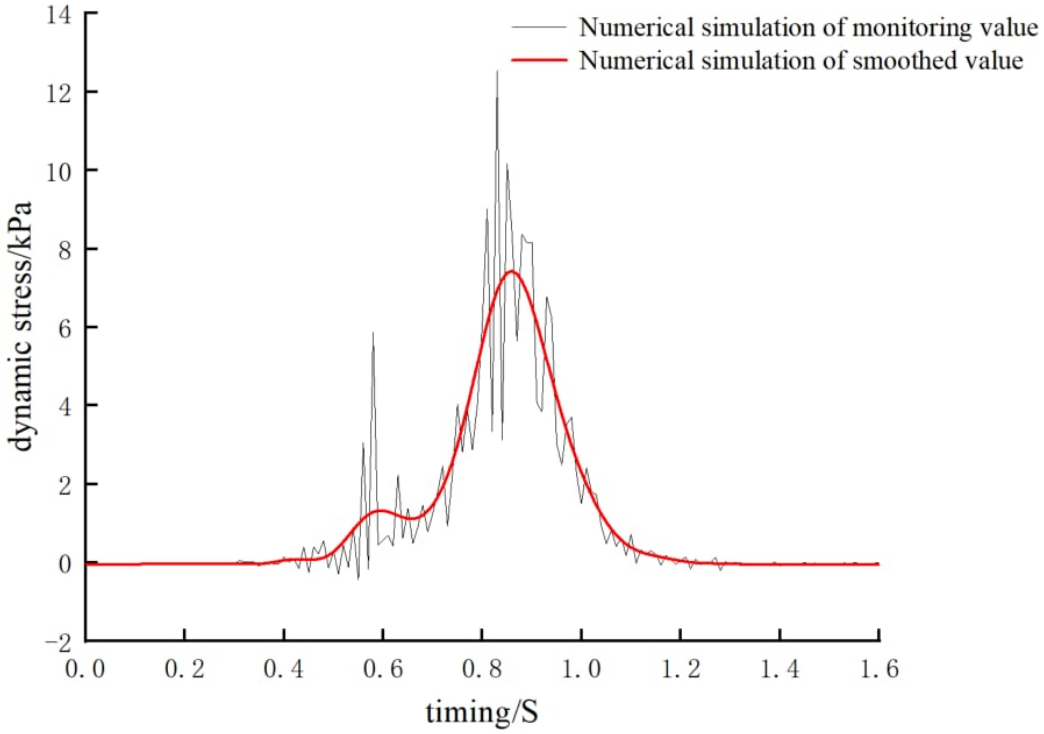

Figure 19. Numerically computed dynamic stress–time history curves.

The number of smoothing iterations was determined through a sensitivity analysis rather than solely by visual inspection. Specifically, different iteration numbers were evaluated by examining the reduction in high-frequency fluctuations, the relative variation in peak dynamic stress between successive iterations, the stability of peak occurrence time, and the preservation of the overall stress–time history. The selected iteration number was the minimum number required to achieve a stable smoothed response without excessive attenuation of the main stress peaks. Based on these criteria, 10 iterations were retained for the field measurements, which exhibited stronger fluctuations, whereas 6 iterations were used for the numerical results, which showed comparatively weaker high-frequency fluctuations. The smoothed curves were used primarily to compare the overall dynamic stress response trends rather than to represent the unfiltered peak stress amplitudes.

3. Results and Discussion

As the direct supporting structure of the pavement, the upper subgrade has a significant impact on the dynamic response of the roadbed under moving vehicle loads. Here, a numerical model of the dynamic response of a roadbed under different vehicle operating conditions, including the effects of vehicle weight and speed on the dynamic dissipation of geocells, is established. Furthermore, taking a vehicle weight of 43 t and a speed of 60 km/h as an example, the distribution of the wheel stress at different heights above the road surface is studied. Finally, by analyzing the stress distribution state of the geocells in space, the reinforcement mechanism of the geocells under vehicle driving is further studied.

3.1. Numerical Model Validation

Due to the complex surface contact between the tire and the road, there is a certain degree of variability in the dynamic stress at the contact position. To avoid the influence of this variability on the accuracy of the conclusions of this study, only the top surface and the layers below were analyzed for dynamic analysis. Figure 20 shows the variation in the peak values of the numerically calculated dynamic stress and the field test results along the depth of the subgrade for the two different roadbed schemes, with a vehicle weight of 43 t and speed of 20 km/h. This figure shows that the maximum error between the numerical calculations and the field test results for dynamic stress at a speed of 20 km/h is 4.81%. Figure 21 shows the variation in the numerically calculated dynamic stress and the field test results along the depth of the subgrade for the two different roadbed schemes, with a vehicle weight of 43 t and speed of 60 km/h. This figure shows that the maximum error between the numerical calculations and the test results at a speed of 60 km/h is 4.55%. Therefore, it can be concluded that the small difference between the 10-times smoothed field test results and the 6-times smoothed numerical model calculations at the corresponding positions reflects the consistent trend of the original values along the depth of the subgrade. This indicates that the numerical model established in this study is reasonably reliable and that the number of smoothing iterations used for the numerical simulation calculations is appropriate.

The maximum differences between the numerical and field-measured results were 4.81% and 4.55% at 20 and 60 km/h, respectively. These comparisons demonstrate that the numerical model can reasonably reproduce the dynamic stress distribution along the roadbed depth under the tested conditions. It should be noted that the available field data do not permit a further statistical evaluation of the scatter among individual vehicle passages; therefore, the repeatability of the measurements is not quantified using standard deviation in this study.

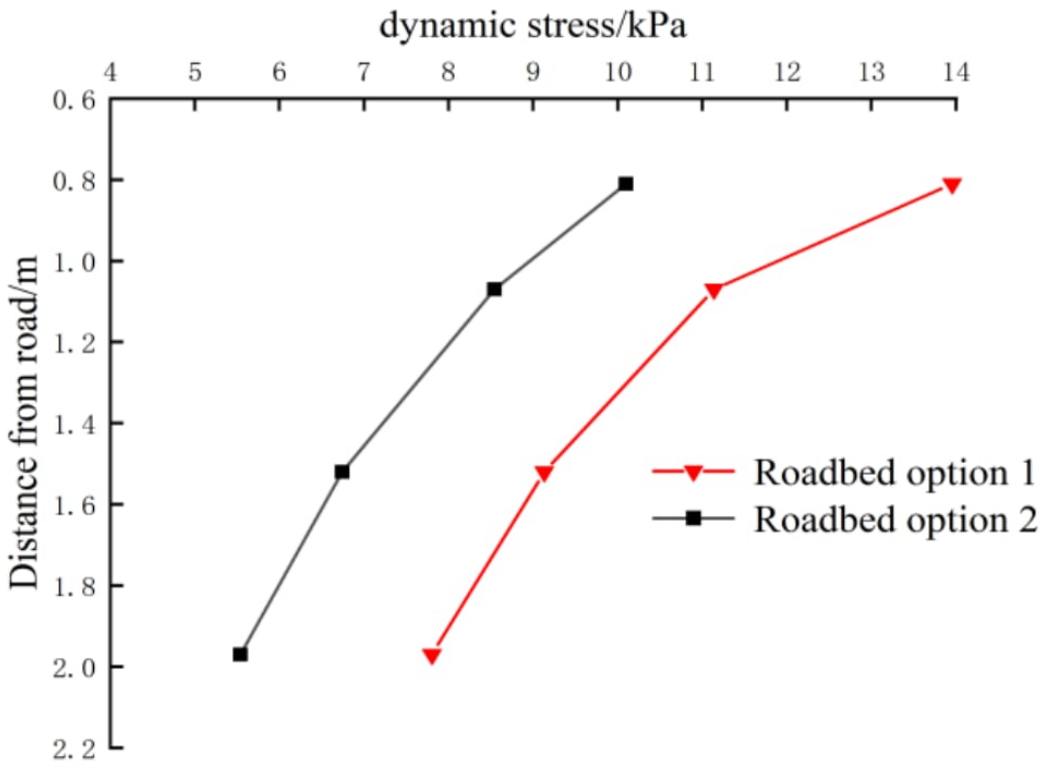

Figure 20. Dynamic stress along the depth direction at a vehicle speed of 20 km/h.

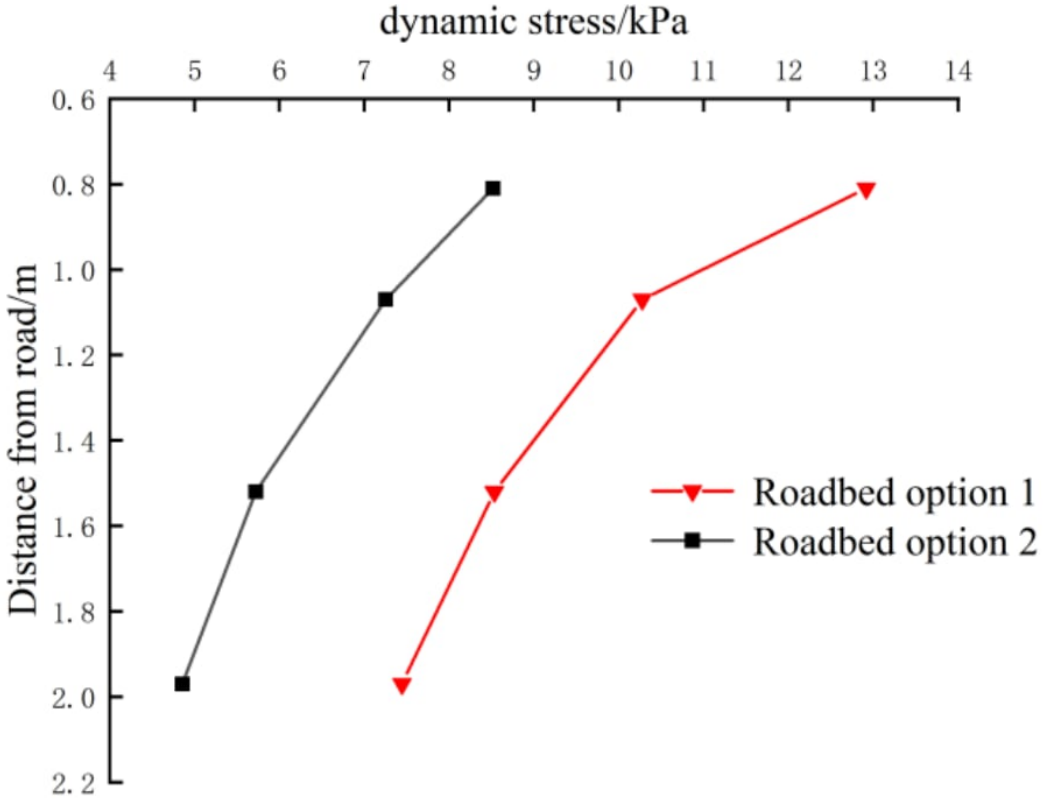

Figure 21. Dynamic stress along the depth direction at a vehicle speed of 60 km/h.

3.2. Impact of Vehicle Load on Roadbed Dynamic Response

Vehicle weight and speed are two important operating conditions that affect the dynamic response of a roadbed. Therefore, studying their impact on roadbed dynamics further clarifies the suitability of using geocell reinforcement for aeolian sand layers in roadbeds.

Figure 22 shows the variation in the dynamic stress along the depth direction of the roadbed under the different vehicle weights for the two different schemes. To maintain a single variable, the vehicle speed in the figure is held constant at 60 km/h. This figure shows that the dynamic stress gradually decreases with increasing depth, starting from the top surface of the roadbed. However, with the linear increase in vehicle weight, the dynamic stress at the same location shows an increasing trend, and this trend becomes more pronounced. Within the range of roadbed heights, for a vehicle weight of 25 t, the dynamic stress of the two roadbed schemes decreases from 37.6~38.3 kPa at the top surface of the subgrade to 3.8~5.6 kPa at the ground surface, with a reduction ranging from 85.4 to 89.9% and an average reduction of 87.7%. For a vehicle weight of 31 t, the dynamic stress decreases from 40.5~41.3 kPa to 4.6~6.9 kPa, with a reduction ranging from 83.3 to 88.6% and an average reduction of 86.0%. For a vehicle weight of 37 t, the dynamic stress decreases from 45.4~46.3 kPa to 5.5~8.5 kPa, with a reduction ranging from 81.6 to 87.9% and an average reduction of 84.8%. For a vehicle weight of 43 t, the dynamic stress decreases from 54.4~55.6 kPa to 6.7~10.1 kPa, with a reduction ranging from 81.8 to 87.7% and an average reduction of 84.8%. For a vehicle weight of 49 t, the dynamic stress decreases from 66.6~68.4 kPa to 9.2~13.3 kPa, with a reduction ranging from 80.6 to 86.2% and an average reduction of 83.4%. The main attenuation of dynamic stress under different vehicle weights occurs within the range of roadbed height, and under the same vehicle weight conditions, the dynamic stress of Scheme 2 is always lower than that of Scheme 1. This indicates that the geocell reinforcement scheme for aeolian sand layers on the roadbed has a better dynamic reduction performance than does the original gravel soil scheme under different vehicle weight conditions.

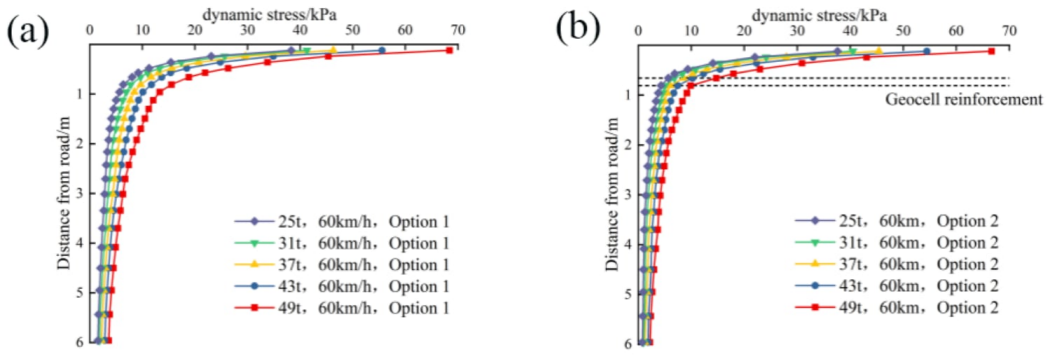

(**a**) Option 1 (**b**) Option 2

Figure 22. Variation curve of the dynamic stress along the depth direction of the roadbed under the different vehicle weights.

Figure 23 shows the variation in the dynamic stress along the depth direction of the roadbed under different vehicle speeds for the two different schemes with a vehicle weight of 43 t. The figure shows that as the vehicle speed increases, the dynamic stress decreases, which is consistent with the conclusions of Assogba et al. [44]. This is because for dynamic deformation, time effect must be considered (i.e., stress-wave propagation; the propagation speed of force is equivalent to the propagation speed of vibration). The faster the longitudinal vehicle speed is, the shorter the duration of action on the road surface, and the smaller the vertical deformation, resulting in a smaller vertical stress. Notably, this does not mean that the dynamic load is smaller than the static load. The stress amplitudes shown in the

figure are smoothed and are not the actual measured dynamic stress amplitudes. The data obtained through this smoothing processing method are suitable for comparing dynamic stresses but not for directly comparing them with the roadbed stress under static loading. In addition, within the height range from the top surface of the roadbed to the surface of the subgrade, when the vehicle speed is 20 km/h, the dynamic stress decreases from 60.2~61.3 kPa at the top surface of the roadbed to 8.1~10.3 kPa at the surface of the subgrade, with a reduction ranging from 83.2 to 86.5% and an average reduction of 84.9%. When the vehicle speed is 60 km/h, the dynamic stress decreases from 54.4~55.6 kPa to 6.7~10.1 kPa, with a reduction ranging from 81.8 to 87.7% and an average reduction of 84.8%. When the vehicle speed is 100 km/h, the dynamic stress decreases from 45.4~46.9 kPa to 5.1~9.6 kPa, with a reduction ranging from 79.5 to 88.8% and an average reduction of 84.2%. The attenuation of dynamic stress caused by vehicles under different speed conditions mainly occurs within the height range of the roadbed. In addition, under the same speed conditions, the dynamic stress of Scheme 2 is always smaller than that of Scheme 1, indicating that under different speed conditions, the geocell-reinforced aeolian sand roadbed scheme has a better dynamic reduction performance than the original gravel roadbed scheme [45,46].

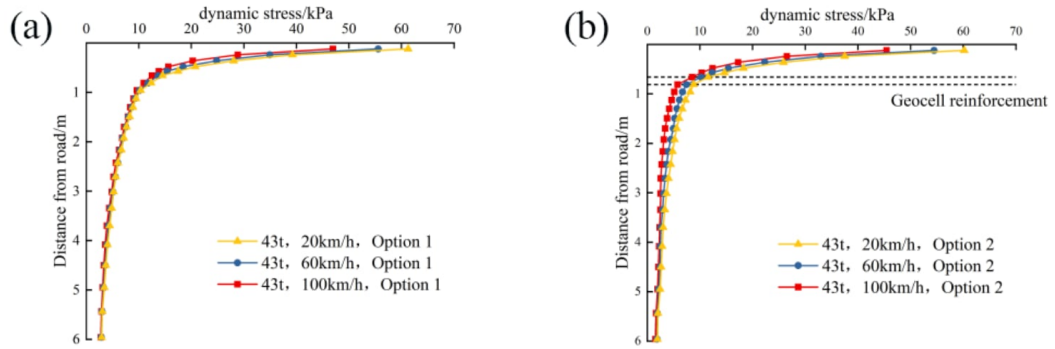

(**a**) Option 1 (**b**) Option 2

Figure 23. Variation curve of the dynamic stress along the depth direction of the roadbed at the different vehicle speeds.

Combining the dynamic attenuation processes of the two design schemes in Figures 22 and 23, it can be seen that the geocell-reinforced aeolian sand subgrade and the gravel subgrade both exhibit a better dynamic reduction performance than the gravel subgrade under the different traffic conditions tested. This dynamic reduction effect may be attributed to two reasons. First, the modulus of the geocell is much greater than that of aeolian sand and gravel, and the presence of the geocell structure in the aeolian sand provides lateral confinement, increasing the stiffness of the subgrade and thus enhancing its ability to homogenize dynamic stress peaks. Second, the geocell has a high tensile strength, causing the geocell–aeolian sand composite layer to form a concave surface similar to a net under vertical loads. The tension around the concave surface reduces the vertical force below the concave surface, resulting in a decrease in the force transmitted to the lower layers compared to the upper vertical force. This is known as the net effect [47,48], which manifests as a decrease in the vertical stress in the lower layers after passing through the geocell–aeolian sand composite layer. Therefore, from a dynamic perspective, the use of the geocell-reinforced aeolian sand subgrade scheme as a replacement for the original gravel subgrade scheme is recommended.

To further analyze the influence of traffic conditions on the dynamic response of the roadbed, taking the dynamic stress on the top surface of the subgrade as an example, the effects of vehicle weight and vehicle speed on the roadbed dynamics are analyzed. Figures 22 and 23 show that when the vehicle weight increases from 25 t to 49 t, the mass

increases by 96%. Correspondingly, the dynamic stress on the top surface of the subgrade increases from 37.6~38.3 kPa to 66.6~68.4 kPa, with an increase ranging from 77.1 to 78.6% and an average increase of 77.9%. However, an increase in the vehicle speed from 20 km/h to 100 km/h is an increase of 400%. Correspondingly, the dynamic stress on the top surface of the subgrade decreases from 60.2~61.3 kPa to 45.4~46.9 kPa, with a reduction ranging from 23.5 to 24.6% and an average reduction of 24.1%. This indicates that the variation in vehicle weight has a greater impact on roadbed dynamics than does the variation in vehicle speed [49,50].

To further illustrate the relationship between vehicle speed and roadbed dynamic stress, the vertical dynamic stresses at the top surface of the base course were extracted for the conventional gravel-soil roadbed (Scheme 1) and the geocell-reinforced aeolian sand roadbed (Scheme 2) at vehicle speeds of 20, 60, and 100 km/h, with a constant vehicle mass of 43 t. The results are presented in Figure 24, using the same stress evaluation procedure as that employed in Figure 24.

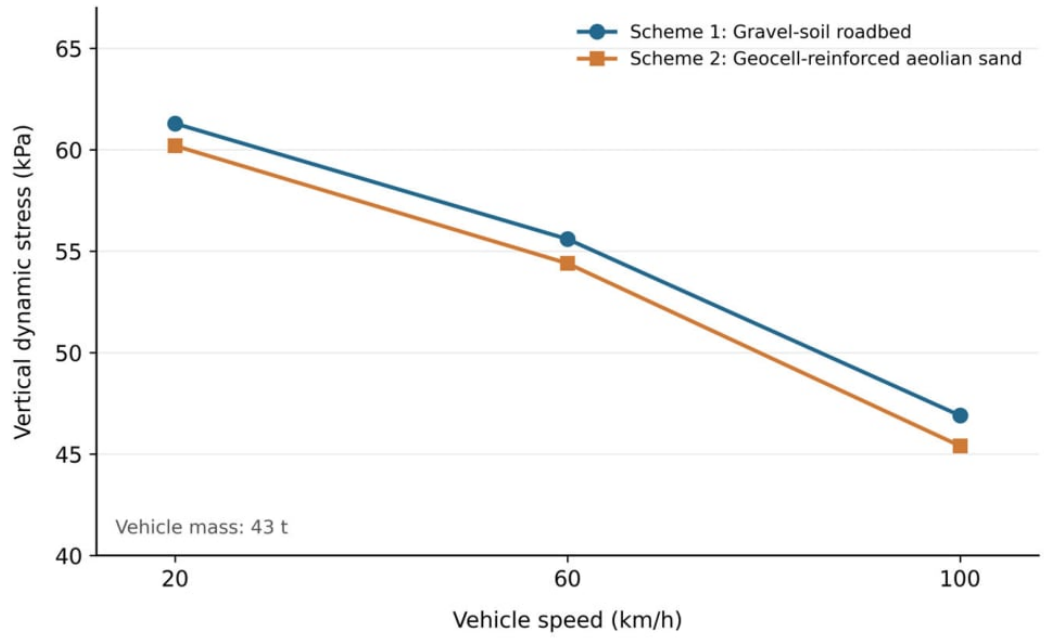

Figure 24. Effect of vehicle speed on vertical dynamic stress at the top surface of the base course (vehicle mass: 43 t).

As shown in Figure 24, the vertical dynamic stresses in both roadbed configurations decrease with increasing vehicle speed. When the vehicle speed increases from 20 to 100 km/h, the dynamic stresses decrease from 61.3 to 46.9 kPa for Scheme 1 and from 60.2 to 45.4 kPa for Scheme 2, corresponding to reductions of approximately 23.5% and 24.6%, respectively. The average reduction is approximately 24.1%. Furthermore, Scheme 2 consistently exhibits lower dynamic stresses than Scheme 1 at the same vehicle speeds, indicating that geocell reinforcement improves the dynamic stress response of the aeolian sand roadbed under the investigated conditions.

To further study the influence of traffic conditions on the dynamic reduction effect of the geosynthetic grid-reinforced aeolian sand composite structural layer, the variation in the dynamic stress difference between Scheme 1 and Scheme 2 along the depth direction of the roadbed is analyzed. Figure 25 shows the variation curves of the dynamic stress difference along the depth direction of the roadbed under different vehicle weights and speeds for the two schemes. Figure 25 shows that on the upper part of the geosynthetic grid-reinforced aeolian sand subgrade, the dynamic stress difference between the two schemes

increases with distance from the road surface; on the lower part of the geosynthetic grid-reinforced aeolian sand subgrade, the dynamic stress difference between the two schemes decreases with distance from the road surface. This indicates that the dynamic reduction effect of the geosynthetic grid-reinforced aeolian sand composite structural layer is the strongest near its source and gradually decreases with increasing distance. Additionally, the dynamic reduction effect of the geosynthetic grid is not only significant in the lower part, as conventionally believed, but also has a noticeable effect on the adjacent upper part. Figure 25a shows that as the vehicle weight increases, the dynamic stress difference between the two schemes gradually increases, indicating that a higher vehicle weight results in a stronger dynamic reduction effect of the geosynthetic grid-reinforced aeolian sand composite structural layer. Furthermore, when the vehicle weight is 25 t, the dynamic stress difference in the upper part of the geosynthetic grid is greater than that in the lower part. When the vehicle weight increases to 37 t, the dynamic stress difference in the lower part of the geosynthetic grid is greater than that in the upper part. This suggests that the geosynthetic grid has a better dynamic reduction effect on the upper part when the vehicle weight is smaller and a better effect on the lower part when the vehicle weight is larger. Figure 25b shows that as the vehicle speed increases, the dynamic stress difference between the two schemes generally increases, indicating that a higher vehicle speed results in a stronger dynamic reduction effect of the geosynthetic grid-reinforced aeolian sand composite structural layer. Additionally, at different vehicle speeds, the dynamic reduction effect of the geosynthetic grid-reinforced aeolian sand layer is better in the lower part of the subgrade. Therefore, the use of a geosynthetic grid-reinforced aeolian sand composite structural layer in heavy-duty or high-speed highways is recommended. Furthermore, considering the gradual attenuation of dynamic stress along the depth of the roadbed, it can be concluded that the application of a geosynthetic grid-reinforced aeolian sand (as it is used in the subgrade with a geosynthetic grid-gravel base) composite structural layer in the upper part of the road surface structure is also worth studying.

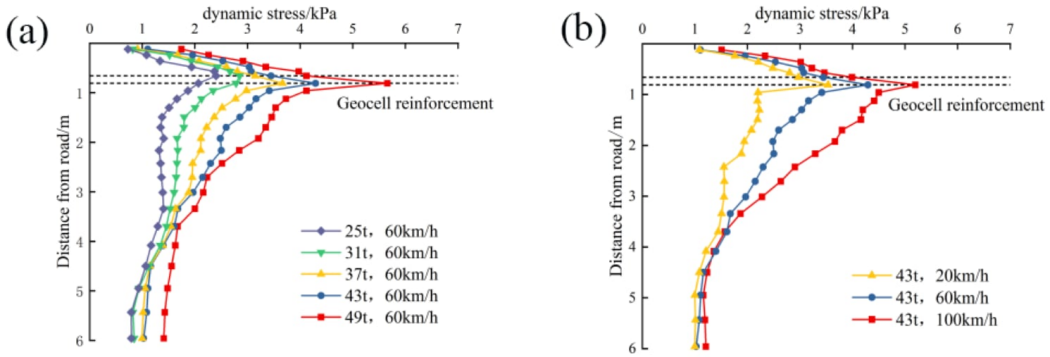

(**a**) Vehicle weight (**b**) Vehicle speed

Figure 25. Variation curves of the dynamic stress difference along the depth direction of the roadbed for the two schemes under different traffic conditions.

3.3. Roadbed Stress Distribution

Figures 26 and 27 show the vertical dynamic stress distribution of different layers in the subgrade under vehicle loading. Figure 26 shows that stress peaks appear below each wheel on the subgrade surface, and the stress decreases rapidly with increasing distance from the wheel. In particular, there are double peaks in the vertical stress below the middle and rear wheels on the base layer surface, and the inner peak stress is greater than the outer peak stress. This indicates that under driving conditions, there are differences in stress below the dual tires at positions closer to the road surface, and the stress caused by the tire on the inner side of the vehicle is greater than that caused by the tire on the

outer side. Figure 26 shows that the stress difference below the dual tires on the base layer surface gradually decreases with increasing distance from the road surface, resulting in the merging of the double peaks into a single peak. The stress distribution in the wheel area on the plane also becomes smoother, indicating that the stress caused by the vehicle is gradually homogenized after passing through the highway structural layers. Figures 28–30 show that near the top of the geosynthetic grid-reinforced aeolian sand layer, the peak stress difference in Scheme 2 is smaller than that of Scheme 1 on the same plane, and overall, the stress peaks of Scheme 2 are smaller than those of Scheme 1. This indicates that the geosynthetic grid-reinforced aeolian sand structural layer has the effect of homogenizing and reducing stress peaks.

According to the results of the projection of the maximum stress envelope surface on the longitudinal plane shown in Figures 26–30, when the vertical dynamic force caused by the vehicle is transferred to the top surface (0.66 m) of the geocell unit, the maximum stress appears below the rear axle of the vehicle. After the reduction in the geocell–aeolian sand composite structural layer, the maximum vertical stress in the subgrade below it (0.81 m) appears near the middle axis. In the subgrade without geocell units, the phenomenon of the maximum stress occurring near the middle axis arises when the distance from the road surface reaches 0.96 m. This indicates that with increasing distance from the road surface, the maximum stress tends to shift below the middle axis, and the geocell–aeolian sand composite structural layer accelerates this process. By comparing the projections of the maximum stress envelope surface at different distances from the road surface in the transverse plane in Figures 26–30, it can be seen that with increasing distance from the road surface, the trend of the peak stress location shifts toward the middle axis.

According to the projections of the envelope surface of the maximum stress at different depths from the road surface in the transverse and longitudinal planes, as the depth increases, the peak stress values at different depths of the subgrade tend to concentrate toward the middle of the vehicle. This is mainly because the forces acting on each wheel diffuse along a certain spreading angle. After passing through various structural layers, the superposition effect of the forces between the wheels leads to an increase in the stress between the two axles and between the two wheels of a single axle. This is manifested by the fact that the maximum stress position in the subgrade caused by the vehicle will concentrate toward the lower middle position of the vehicle farther than a certain distance from the road surface, indicating a centering effect of vertical stress.

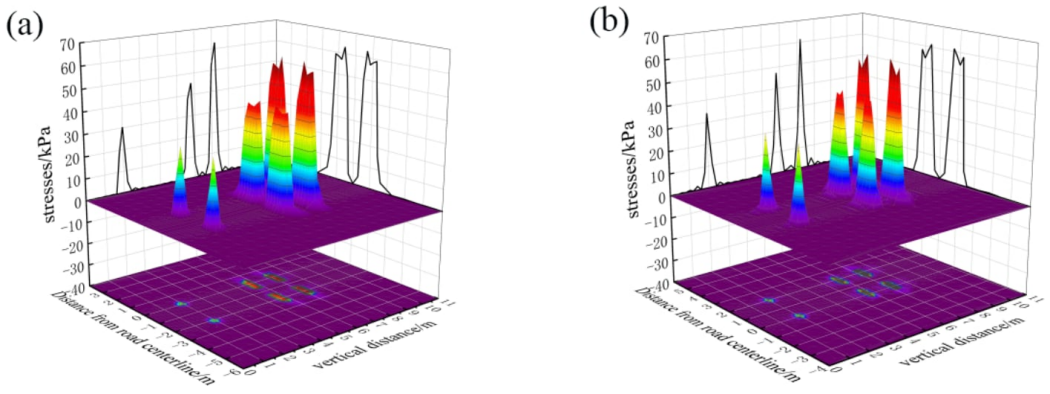

(**a**) Without geocells (**b**) With geocells

Figure 26. Stress distribution of the roadbed 0.12 m from the road surface.

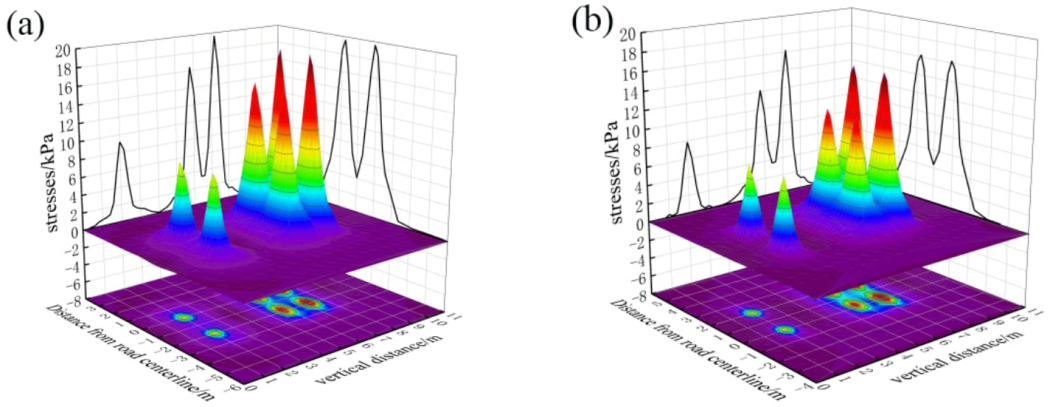

(**a**) Without geocells (**b**) With geocells

Figure 27. Stress distribution of the roadbed 0.48 m from the road surface.

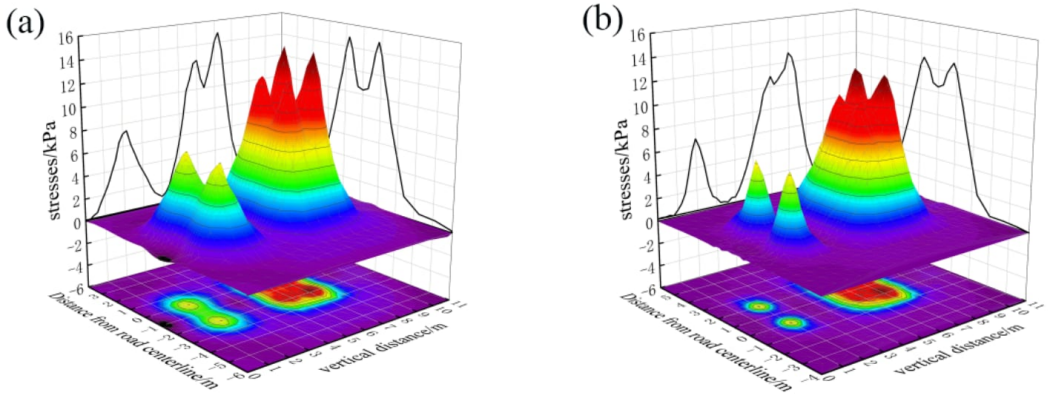

(**a**) Without geocells (**b**) With geocells

Figure 28. Stress distribution of the roadbed 0.66 m from the road surface.

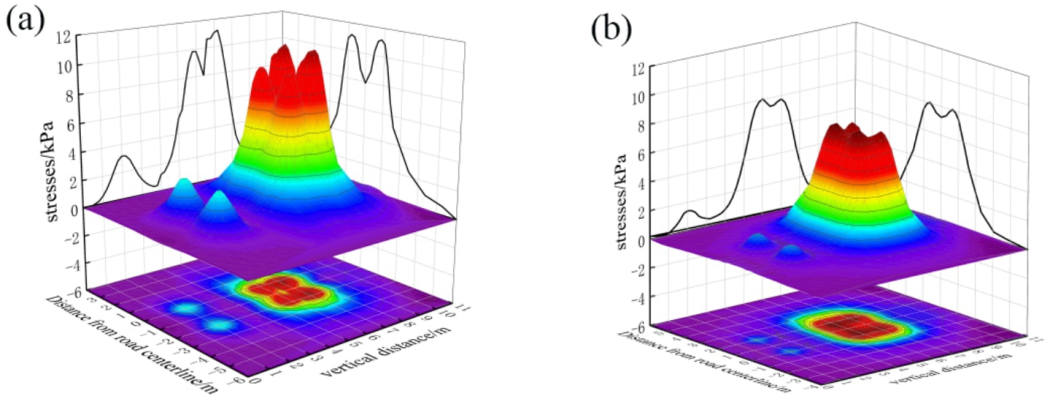

(**a**) Without geocells (**b**) With geocells

Figure 29. Stress distribution of the roadbed 0.81 m from the road surface.

In addition, Figures 26–30 show that as the distance from the road surface increases, the decay rate of the peak stress under the front axle wheel is faster than that under the middle and rear axle wheels. This may be related to the overlap of stress decay. The front axle is far from the middle axle, so it cannot overlap with the stress under the middle and rear axles, resulting in a significantly faster decay rate of the stress under the front axle compared to the overlapping stress under the middle and rear axles.

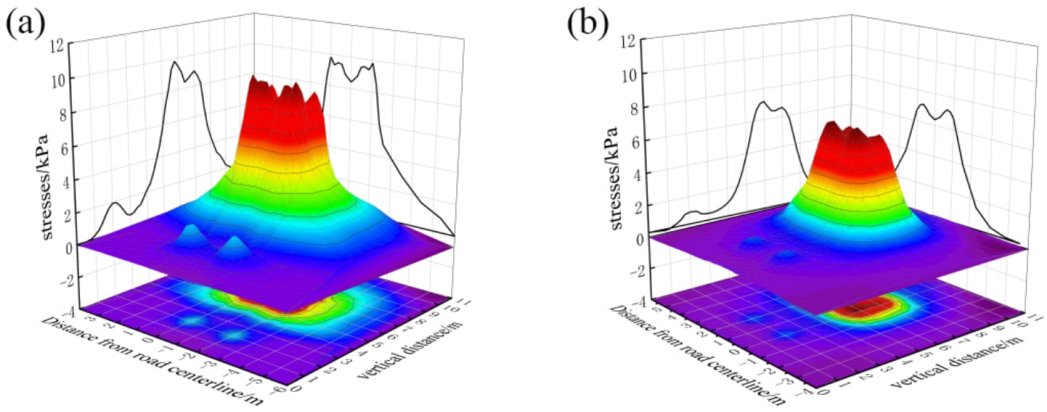

(**a**) Without geocells (**b**) With geocells

Figure 30. Stress distribution of the roadbed 0.96 m from the road surface.

3.4. Analysis of the Dynamic Deformation Process of Geogrid Cells

During vehicle operation, the dynamic deformation process of a single geocell can be divided into three stages: before vehicle approach, during vehicle loading, and after vehicle departure. Figures 31–33 show this dynamic deformation process in the roadbed beneath the wheel paths, as viewed from above, from the left, and from the front, respectively.

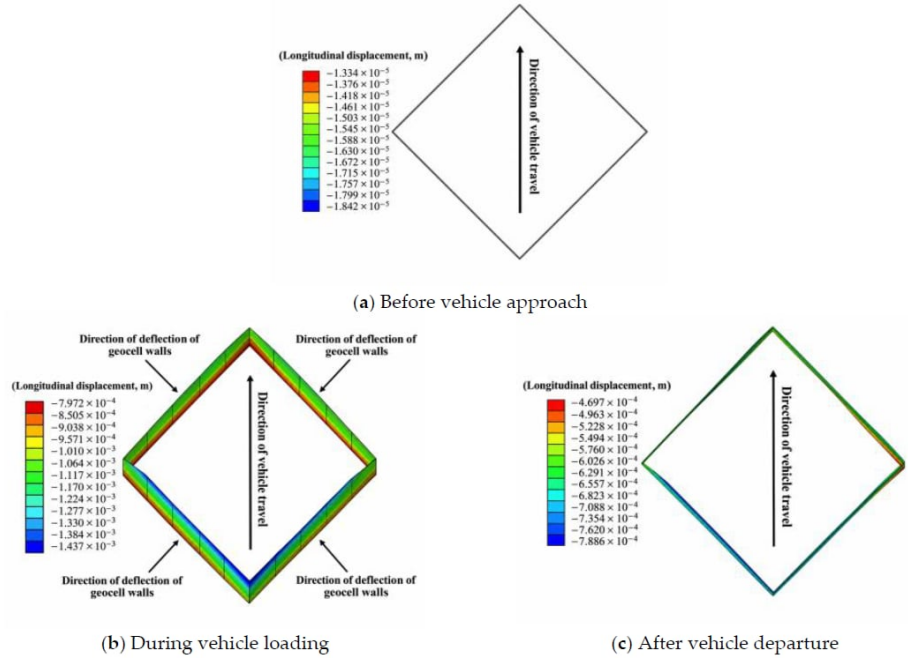

(**a**) Before vehicle approach

(**b**) During vehicle loading (**c**) After vehicle departure

Figure 31. Top view of the dynamic changing process of the geocell (magnified by 100 times).

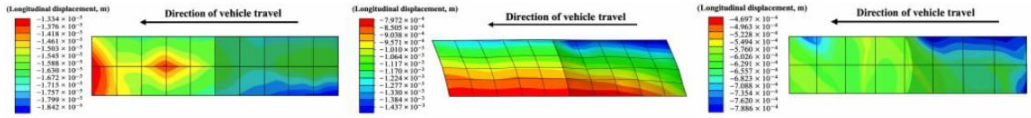

(**a**) Before vehicle approach (**b**) During vehicle loading (**c**) After vehicle departure

Figure 32. Left view of the dynamic changing process of the geocell (magnified by 100 times).

As shown in Figure 31, before vehicle approach, the geocell exhibits a planar shape (typically a regular hexagon) and largely maintains its initial position. During vehicle loading, the four surrounding walls deflect primarily parallel to the geocell's length, and this deflection occurs at an acute angle to the direction of vehicle travel. Additionally, wall

displacement increases along the longitudinal axis of the road. After vehicle departure, the geocell deformation progressively rebounds.

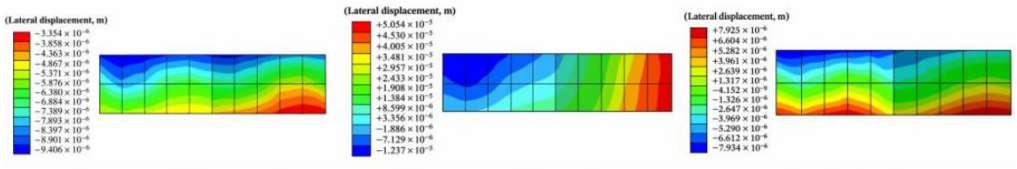

(**a**) Before vehicle approach (**b**) During vehicle loading (**c**) After vehicle departure

Figure 33. Front view of the process of dynamic changing process in the geocell (magnified by 100 times).

As shown in Figure 32, before vehicle approach, the front and rear weld lines of the geocell remain vertical with minimal longitudinal deformation. During vehicle loading, the geocell structure tilts forward as a whole. The front weld line becomes concave while the rear becomes convex, indicating greater inclination in the upper half of the cell wall compared to the lower half. The numerical results indicate that the geocell walls undergo spatially varying displacement and tilting under moving vehicle loads. The membrane elements capture the in-plane tensile response and the associated deformation of the geocell walls. However, because bending stiffness is neglected in the adopted membrane formulation, bending moments and bending stresses cannot be directly evaluated in the present model. The tilt occurs because vehicle-induced dynamic soil pressure propagates as additional stress through the roadbed in both horizontal and vertical directions. Consequently, even distant cell walls experience this dynamic stress before the vehicle's arrival. Furthermore, the aforementioned variation in dynamic stress with depth shows decreasing magnitude at greater depths, indicating higher additional dynamic soil pressure on the geocell's upper portion than on its lower portion. This results in gradually decreasing lateral earth pressure along the geocell's height. Under this uneven pressure distribution, the geocell tilts forward. After vehicle departure, the deformation gradually recovers as the additional dynamic soil pressure dissipates.

As shown in Figure 33, the geocell units exhibit negligible deformation or displacement in the transverse direction throughout the vehicle's passage. Consistent with Figure 32, longitudinal deformation under moving vehicle loads substantially exceeds transverse deformation.

In summary, the dynamic deformation behavior of geocells under moving vehicle loads fundamentally differs from that under static or conventional vertical dynamic loads. When subjected to moving vehicles, geocells exhibit longitudinal deflection and forward tilting, whereas transverse deformation remains negligible. This anisotropic response contrasts sharply with the deformation patterns observed under static or vertical dynamic loading conditions.

A limitation of the present study is that the two roadbed configurations differ in both filling material and reinforcement arrangement. Therefore, the individual contribution of geocell reinforcement cannot be isolated from the effect of replacing gravelly soil with aeolian sand. An additional unreinforced aeolian sand configuration with the same layer thickness and material properties as Scheme 2 would be required to quantify the independent reinforcement effect. Future investigations should include such a reference configuration to further distinguish the effects of material replacement and geocell reinforcement.

4. Conclusions

4.1. Main Conclusions

Considering the dynamic coupling between the vehicle body, vehicle wheels, and roadway, a full-scale three-dimensional dynamic model was established to study the dynamic response of aeolian sand-reinforced roadbeds with geocell chambers under traffic loads. Field driving tests were conducted on the newly constructed Almaty–Urumqi Expressway to measure the dynamic response data of the subgrade, which were used to validate the established three-dimensional dynamic model. The following conclusions were drawn:

1. A three-dimensional finite element model was established to account for the dynamic coupling between the vehicle body, tires and subgrade, and was validated using on-site driving tests on the S21 Desert Motorway. Within the validated range of vehicle mass and speed, the model was able to reproduce the variation in dynamic subgrade stresses reasonably well, thereby providing a numerical analysis method for investigating the dynamic response of reinforced eolian sand subgrades under moving vehicle loads.
2. The vertical dynamic stresses induced by vehicle loads attenuate significantly with increasing subgrade depth. Within the 0.96 m pavement–subgrade structure investigated in this study, dynamic stresses exhibited a pronounced depth-dependent attenuation. An increase in vehicle mass leads to an overall increase in dynamic stresses, whilst the effect of changes in vehicle speed on dynamic stresses depends on the stress evaluation criteria and model conditions employed.
3. Compared with conventional gravelly soil subgrades, geocell-reinforced eolian sand subgrades exhibit lower dynamic stresses and a more uniform spatial distribution of stresses under the operating conditions studied. The geocell reinforcement not only affects stress transmission beneath the cells but also alters the stress distribution in the adjacent upper regions, reflecting the combined effect of lateral confinement and load diffusion.
4. Under the action of moving vehicle loads, the geocells exhibited pronounced longitudinal deflection and tilting deformation, with longitudinal deformation exceeding transverse deformation; this indicates that the moving characteristics of vehicle loads influence the dynamic stress and deformation behavior of the geocells. The research findings provide a reference for the design of reinforced eolian sand subgrades for desert roads; however, further verification is required regarding their applicability under different geocell interface conditions and under long-term cyclic loading.

4.2. Limitations and Future Work

This paper establishes a three-dimensional finite element model for the coupled dynamic interaction between vehicle, wheel and road, and verifies its reliability. The study investigates the dynamic response of the subgrade, the reinforcement effect of geocells on the subgrade, and the reinforcement mechanism. However, there are certain limitations:

1. Although the aeolian sand was modeled using the Mohr–Coulomb elastoplastic model, constant elastic parameters were adopted and the stress-dependent stiffness, cyclic hardening/softening, and long-term accumulated plastic deformation of granular soils were not explicitly considered.
2. The limitations arising from the simplified tire model have not been discussed.
3. Lack of durability testing, such as long-term fatigue resistance tests and long-term deformation performance assessments.
4. The frequency-domain characteristics of the field measurements were not fully investigated. Although the theoretical axle-passage frequencies were below the Nyquist frequency corresponding to the adopted sampling rate of 100 Hz, the original un-

processed signals and sensor-specific frequency-response calibration records were unavailable. Therefore, the raw-signal FFT spectra and the frequency response of the complete measurement system could not be independently reconstructed. Consequently, the field measurements were primarily used to evaluate the overall dynamic response and depth-dependent stress distribution, rather than to characterize high-frequency tire–road contact transients.

5. The embedded-element constraint as-sumes compatible deformation between the geocell and surrounding soil, neglecting interfacial sliding and separation. In addition, the linear elastic membrane model does not fully capture the nonlinear and time-dependent tensile behavior of HDPE. Variations in interface friction and geocell tensile stiffness may affect confinement efficiency and the predicted stress redistribution.

Future work will continue to be carried out on this basis:

1. Test cyclic fatigue with accelerated pavement testing.
2. Model seasonal moisture variation. Pay attention to the effects of temperature and humidity on the model.
3. Explore cell geometries aligned with traffic direction.
4. Future research will employ higher sampling rates for data acquisition and specialized frequency response identification techniques to address stress wave propagation issues.

Author Contributions: Conceptualization, J.L. and J.K.; methodology, J.L.; software, J.K.; validation, J.K.; investigation, Y.Y.; data curation, Y.Y.; writing—review and editing, J.X.; visualization, J.K.; supervision, J.P.; project administration, J.Z. All authors have read and agreed to the published version of the manuscript.

Funding: This research was funded by the Technology Research and Development Project of Xinjiang Transportation Investment (Group) Co., Ltd. (grant numbers ZKXFWCG2024080484 and XJJTZKX-FWCG-202411-0738), and the First Batch of Scientific Research Projects of Xinjiang Transportation Investment (Group) Co., Ltd. in 2023 (grant number XJJTZKX-FWCG-202401-0043).

Data Availability Statement: The data supporting the findings of this study are available from Xinjiang Transportation Research Institute Co., Ltd. However, restrictions apply to the availability of these data, which were used under license for the current study and are therefore not publicly available. The data may be made available upon reasonable request and with the permission of Xinjiang Transportation Research Institute Co., Ltd.

Conflicts of Interest: All authors worked for company Xinjiang Transportation Science Research Institute Co., Ltd.

Abbreviations

The following abbreviations are used in this manuscript:

HDPE	High-Density Polyethylene
RSM	Reinforced Soil Mass
DXF	Drawing Exchange Format
FFT	Fast Fourier Transform
FRF	Frequency Response Function
CBR	California Bearing Ratio

References

1. Arias, L.J.; Inti, S.; Tandon, V. Influence of Geocell Reinforcement on Bearing Capacity of Low-Volume Roads. *Transp. Dev. Econ.* **2020**, *6*, 5. [CrossRef]
2. Banerjee, L.; Chawla, S.; Kumar Dash, S. Application of geocell reinforced coal mine overburden waste as subballast in railway tracks on weak subgrade. *Constr. Build. Mater.* **2020**, *265*, 120774. [CrossRef]

3. Inti, S.; Tandon, V. Design of geocell reinforced roads through fragility modeling. *Geotext. Geomembr.* **2021**, *49*, 1085–1094. [CrossRef]
4. Punetha, P.; Nimbalkar, S. Performance improvement of ballasted railway tracks using three-dimensional cellular geoinclusions. *Geotext. Geomembr.* **2022**, *50*, 1061–1082. [CrossRef]
5. Qi, H.; Zhang, X.; Liu, J.; Zhang, T.; Lv, G.; Cui, L.; Xie, Q. Study on Deformation Characteristics of Low-highway Subgrade under Traffic Load. *Appl. Sci.* **2022**, *12*, 3406. [CrossRef]
6. Ari, A.; Misir, G. Three-dimensional numerical analysis of geocell reinforced shell foundations. *Geotext. Geomembr.* **2021**, *49*, 963–975. [CrossRef]
7. Shadmand, A.; Ghazavi, M.; Ganjian, N. Load-settlement characteristics of large-scale square footing on sand reinforced with opening geocell reinforcement. *Geotext. Geomembr.* **2018**, *46*, 319–326. [CrossRef]
8. Tanyu, B.F.; Aydilek, A.H.; Lau, A.W.; Edil, T.B.; Benson, C.H. Laboratory evaluation of geocell-reinforced gravel subbase over poor subgrades. *Geosynth. Int.* **2013**, *20*, 47–61. [CrossRef]
9. Tavakoli Mehrjardi, G.; Behrad, R.; Moghaddas Tafreshi, S.N. Scale effect on the behavior of geocell-reinforced soil. *Geotext. Geomembr.* **2019**, *47*, 154–163. [CrossRef]
10. Saride, S.; Rayabharapu, V.K.; Vedpathak, S. Evaluation of Rutting Behaviour of Geocell Reinforced Sand Subgrades Under Repeated Loading. *Indian Geotech. J.* **2014**, *45*, 378–388. [CrossRef]
11. Gao, B.; Liu, X.; Liu, J.; Song, L.; Shi, Y.; Yang, Y. Field Characterization of Dynamic Response of Geocell-Reinforced Aeolian Sand Subgrade under Live Traffic. *Appl. Sci.* **2023**, *13*, 864. [CrossRef]
12. Latha, G.M.; Manju, G.S. Seismic Response of Geocell Retaining Walls Through ShakingTable Tests. *Int. J. Geosynth. Ground Eng.* **2016**, *2*, 1–15. [CrossRef]
13. Saride, S.; Gowrisetti, S.; Sitharam, G.T.; Puppala, A.J. Numerical simulation of geocell-reinforced sand and clay. *Proc. Inst. Civ. Eng.-Ground Improv.* **2009**, *162*, 185–198. [CrossRef]
14. Hegde, S. Experimental and numerical studies on footings supported on geocell reinforced sand and clay beds. *Int. J. Geotech. Eng.* **2013**, *7*, 346–354. [CrossRef]
15. Hegde, A.; Sitharam, T.G. 3-Dimensional numerical modelling of geocell reinforced sand beds. *Geotext. Geomembr.* **2015**, *43*, 171–181. [CrossRef]
16. Hegde, A.M.; Sitharam, T.G. Three-Dimensional numerical analysis ofgeocell reinforced soft clay beds byconsidering the actual geometry ofgeocell pockets. *Can. Geotech. J.* **2015**, *52*, 1396–1407.
17. Zhang, S.H.; Li, Z.Y.; Peng, D.; Chen, Z.M. Study of statie property of aeolian sand used as roadbed. *Rock Soil Mech.* **2007**, *28*, 2511–2516. [CrossRef]
18. Li, Z.N.; Jin, C.N. Test on Dry Compaction of Typical Earth Subgrade in Xinjiang. *China J. Highw. Transp.* **2007**, *20*, 23–28. [CrossRef]
19. Venkateswarlu, H.; Hegde, A. Behavior of geocell reinforced bed under vibration loading: 3D numerical studies. *Geosynth. Int.* **2022**, *30*, 651–670. [CrossRef]
20. Wu, M.; Tian, W.; Liu, F.; Yang, J. Dynamic behavior of geocell-reinforced rubber sand mixtures under cyclic simple shear loading. *Soil Dyn. Earthq. Eng.* **2023**, *164*, 107595. [CrossRef]
21. Tafreshi, M.S.; Dawson, A. A comparison of static and cyclic loading responses of foundati-ons on geocell-reinforced sand. *Geotext. Geomembr.* **2012**, *32*, 55–68. [CrossRef]
22. Suku, L.; Prabhu, S.S.; Ramesh, P.; Babu, G.L.S. Behavior of geocell-reinforced gran-ular base under repeated loading. *Transp. Geotech.* **2016**, *9*, 17–30. [CrossRef]
23. Siabil, S.M.A.G.; Tafreshi, S.N.M.; Dawson, A.R. Response of pavement foundations incorporating both geocells and expanded polystyrene (EPS) geofoam. *Geotext. Geomembr.* **2020**, *48*, 1–23. [CrossRef]
24. Yang, X.; Han, J.; Pokharel, S.K.; Manandhar, C.; Parsons, R.L.; Leshchinsky, D.; Halahmi, I. Accelerated pavement testing of unpaved roads with geocell-reinforcedsand bases. *Geotext. Geomembr.* **2012**, *32*, 95–103. [CrossRef]
25. Tavakoli Mehrjardi, G.; Moghaddas Tafreshi, S.N.; Dawson, A.R. Pipe response in a geocell-reinforced trench and compaction considerations. *Geosynth. Int.* **2013**, *20*, 105–118. [CrossRef]
26. Albayati, N. Evaluation of the Flexural Stress and Deflection in a Rigid Pavement Utilising Finite Element Analysis. *J. Stud. Civ. Eng.* **2025**, *2*, 108–122. [CrossRef]
27. Saleh, S.A.; Ismael, R.S.; Abas, B.S. Effect of Soil Stabilization on Structural Desig-n of Flexible Pavement. *J. Stud. Civ. Eng.* **2024**, *1*, 36–54. [CrossRef]
28. Shirmohammadi, M.; Hakimi Asiabar, S.; Peyrovi Cheshnasar, M. Dual Transitional Floors and Soil-Structure Synergy: A Paradigm Shift in Seismic Resilience for Hybrid High-Rise Systems. *Adv. Civ. Eng. Environ. Sci.* **2025**, *2*, 62–71. [CrossRef]
29. Research Institute of Highway, Ministry of Transport of the People's Republic of China. *Test Methods of Soils for Highway Engineering (JTG 3430—2020)*; China Communications Press: Beijing, China, 2020.
30. Al-Sanad, H.A.; Ismael, N.F.; Nayfeh, A.J. Geotechnical properties of dune sands in Kuwait. *Eng. Geol.* **1993**, *34*, 45–52. [CrossRef]

31. Al-Taie, A.J.; Al-Shakarchi, Y.J.; Mohammed, A.A. Investigation of geotechnical specifications of sand dune: A case study around Baiji in Iraq. *Int. J. Adv. Res.* **2013**, *1*, 208–215.
32. Yuan, Y.Q.; Wang, X.C. Experimental Study on the Compaction Characteristics of Wind-Deposited Sand. *J. Geotech. Eng.* **2007**, *29*, 360–365.
33. Jaky, J. The Coefficient of Earth Pressure at Rest (A nyugalmi nyomás tényezője). *Magy. Mérn.-ÉS Épít.-Egylet Közlönye* **1944**, *78*, 355–358. (In Hungarian)
34. U.S. Army Corps of Engineers. *Floodwalls and Other Hydraulic Retaining Walls*; Engineer Manual EM 1110-2-2502; U.S. Army Corps of Engineers: Washington, DC, USA, 2022.
35. Komandi, G. The determination of the deflection, contact area, dimensions, and load carrying capacity for driven pneumatic tires operating on concrete pavement. *J. Terramech.* **1976**, *13*, 15–20. [CrossRef]
36. Kumar, S.; Pandey, K.P.; Kumar, R.; Ashok Kumar, A. Effect of ballasting on performance characteristics of bias and radial ply tyres with zero sinkage. *Measurement* **2018**, *121*, 218–224. [CrossRef]
37. Zhao, J.; Li, Z.C.; Guo, X.; Wang, L. Numerical analysis of bitumen-surface highway dynamic response under vehicle loads. *J. Railw. Sci. Eng.* **2012**, *9*, 83–89. [CrossRef]
38. Wang, Y.; Zhao, Y.; Zhang, M.; Fu, G. Influence of bedrock on the dynamic deflection response and dynamic back-calculation results of asphalt pavement: Insights from the numerical simulation of falling weight deflectometer tests. *Constr. Build. Mater.* **2022**, *330*, 127252. [CrossRef]
39. Zhou, T.; Shang, G.M.; Zhai, Y.F. Experimental Analysis on Influencing Factors of Dynamic Characteristicsof Subgrade Gravel Packing Soil. *J. Jilin Univ. (Earth Sci. Ed.)* **2021**, *51*, 1482–1489. [CrossRef]
40. Cai, G.J.; Chen, S.H.; Zhou, Y. Experimental study on influence of coarse grain content on strength and deformation char acteristics of gravel soil. *Water Resour. Hydropower Eng.* **2020**, *1*, 187–195.
41. Liu, D.P.; Yang, X.H.; Liu, H.R.; Wang, J.; Zhang, H.W. Experimental study on influence factors ofgravel soil dynamic elastic modulus and damping ratio. *J. Railw. Sci. Eng.* **2017**, *14*, 264–270. [CrossRef]
42. Jia, M.; Ling, S.; Jie, L.; Bin, W.; Shi, C. Large scale biaxial tensile test on overall mechanicalproperties of HDPE geocell. *J. Changchun Univ. (Nat. Sci. Ed.)* **2021**, *41*, 29–38. [CrossRef]
43. Assogba, O.C.; Sun, Z.; Tan, Y.; Nonde, L.; Bin, Z. Finite-Element Simulation of Instrumented Asphalt Pavement Response under Moving Vehicular Load. *Int. J. Geomech.* **2020**, *20*, 0402000. [CrossRef]
44. Assogba, O.C.; Tan, Y.; Sun, Z.; Lushinga, N.; Bin, Z. Effect of Vehicle Speed and Overload on Dynamic Response of Semi-Rigid Base Asphalt Pavement. *Road Mater. Pavement Des.* **2021**, *22*, 572–602. [CrossRef]
45. Zhang, B.-B.; Liu, J.; Gao, B.; Wang, B.; Ai, Y.-H. The Study on Dynamic Response of Aeolian Sand Embankment Strengthened by Geocell through Field Test. *J. Highw. Transp. Res. Dev. (Engl. Ed.)* **2021**, *15*, 24–35. [CrossRef]
46. Ayasrah, M.; Qiu, H.; Fattah, M.Y.; Mohammed Redha, W.B.; Zhu, B. Experimental Assessment of Geocell-Reinforced Sandy Subgrades under Traffic-Induced Dynamic Loading. *Infrastructures* **2026**, *11*, 38. [CrossRef]
47. Avesani Neto, J.O. Application of the two-layer system theory to calculate the settlements and vertical stress propagation in soil reinforcement with geocell. *Geotext. Geomembr.* **2019**, *47*, 32–41. [CrossRef]
48. Zhang, L.; Zhao, M.; Shi, C.; Zhao, H. Bearing capacity of geocell reinforcement in embankment engineering. *Geotext. Geomembr.* **2010**, *28*, 475–482. [CrossRef]
49. Pokharel, S.K.; Han, J.; Leshchinsky, D.; Parsons, R.L. Experimental Evaluation of Geocell-Reinforced Bases under Repeated Loading. *Int. J. Pavement Res. Technol.* **2018**, *11*, 114–127. [CrossRef]
50. Indraratna, B.; Biabani, M.M.; Nimbalkar, S. Behavior of Geocell-Reinforced Subballast Subjected to Cyclic Loading in Plane-Strain Condition. *J. Geotech. Geoenviron. Eng.* **2015**, *141*, 04014081. [CrossRef]

Disclaimer/Publisher's Note: The statements, opinions and data contained in all publications are solely those of the individual author(s) and contributor(s) and not of MDPI and/or the editor(s). MDPI and/or the editor(s) disclaim responsibility for any injury to people or property resulting from any ideas, methods, instructions or products referred to in the content.